The Congo River plume: Impact of the forcing on the far-field and near-field dynamics

Cléa Denamiel,[1] W. Paul Budgell,[1] and Ralf Toumi[1]

Received 19 April 2012; revised 12 December 2012; accepted 13 December 2012; published 28 February 2013.

[1] The first numerical simulations of the Congo River plume dynamics are presented in this study. The different forcing mechanisms responsible for the seasonal variations of the plume extend are separately analyzed and the Regional Ocean Modeling System (ROMS) is employed to carry out both a process orientated study—with simple baseline simulations and a sensitivity study—with realistic 1 year runs setup in 2005. The baseline model is forced only by the river flow, in the presence of realistic bathymetry. Tides, wind stress, surface heat flux, and ocean boundary conditions are the forcing added to the realistic model. The typical seasonal orientation of the Congo River plume is found to be northward during most of year except for the February–March (FM) season when the plume has a large westward extension (about 800 km) and its area nearly doubles. The northward extension of the plume is explained by a buoyancy-driven upstream coastal flow—due to the unique geomorphology of the Congo River estuary—and the combined influences of the ambient ocean currents and the wind. During the FM season, the surface ocean circulation is driving both (1) the westward extension of the plume and (2) the southward transport of the Nyanga River fresh waters which feed the Congo River plume. In the near-field region of the plume, the presence of the deep Congo canyon has two main effects: (1) its depth increases the intrusion of sea water into the river mouth and (2) its orientation initiates the formation of the upstream flow.

Citation: Denamiel, C., W. P. Budgell, and R. Toumi (2013), The Congo River plume: Impact of the forcing on the far-field and near-field dynamics, *J. Geophys. Res. Oceans*, *118*, 964–989, doi:10.1002/jgrc.20062.

1. Introduction

[2] In the last decades, numerical studies of river plumes have generated considerable research interest and improved the general understanding of the river plume physics. In particular, *Garvine* [1987] simulated the advection of buoyant water by a constant alongshore flow, *Wiseman and Garvine* [1995] described the turbulent mixing processes within a bottom-detached effluent plume and *Fong and Geyer* [2002] characterized the circulation of surface-trapped plumes within the bulge and the coastal current. More recently *MacDonald et al.* [2007] and *O'Donnell et al.* [2008] described the complex relationship between plume thinning/spreading and mixing. *Choi and Wilkin* [2007] highlighted the importance of wind and tidal forcing for the horizontal freshwater dispersal. Moreover, the plume dynamics of the major rivers (in terms of discharge) have now been accessed. A recent numerical study of the Amazon River [*Nikiema et al.*, 2007] reveals that the North Brazil Current is at the origin of the permanent north-westward extension of the plume but that the trade winds and the strong currents associated with the tide also influence the fate of the plume. The numerical study of the impact of the Orinoco River on the Caribbean current [*Chérubin and Richardson*, 2007] confirms that the plume is controlled by the northwest-flowing Guayana Current which acts as a barrier and keeps the turbid Orinoco waters on the shelf. *Schiller et al.* [2011] conclude that the main drivers of the Mississippi plume are the local wind and the interaction of the Loop Current and the associated cyclonic frontal eddies with the shelf waters of the northern Gulf of Mexico. The simulation of the Ganges-Brahmaputra River discharge interannual variations—undertaken between 1992 and 1999 by *Durand et al.* [2011]—reveals significant mixed layer temperature anomalies which potentially influenced the climate of the northern Bay of Bengal.

[3] However, there is no numerical ocean model study of the second largest river in the world and the most significant river of the Southern Hemisphere—the Congo River. The main properties of the Congo River plume have been highlighted by observational studies since the 1980s. *Eisma and Van Bennekom* [1978] describe the plume direction as west-north-west instead of south, as expected at 6°S of latitude due to the Coriolis effect, and *Van Bennekom and Berger* [1984] observe an extension of the plume reaching 800 km offshore during austral summer, when monsoonal

[1]Imperial College, London, UK.

Corresponding author: C. Denamiel, Imperial College, Prince Consort Road., London, SW7 2AZ, UK. (c.denamiel@imperial.ac.uk)

2169-9275/13/10.1002/jgrc.20062

circulation and precipitation reach their maximum intensity. *Jansen et al.* [1984] noticed that the narrowness of the Congo mouth and the presence of a deep canyon—beginning within the river estuary where the bathymetry drops abruptly to 100 m of depth—largely influence the estuarine hydrography. An analysis of the chlorophyll concentration off the Congo River mouth by *Signorini et al.* [1999] reveals that, depending on the seasonal variations of the wind, the ocean circulation and the river discharge, different scenarios of the Congo River plume dispersion can be observed.

[4] These features of the Congo River plume caused by the seasonal variations of a complex environment make the use of ocean models an essential step to understand the formation of this large river plume. For example, the numerical study of the Columbia River with the Regional Ocean Modeling System (ROMS) model during summer 2004 [*Liu et al.*, 2009a, 2009b; *MacCready et al.*, 2009] reveals that the upstream branch of the plume (in the Kelvin wave sense) is purely wind driven. The main objective of our study is thus to discriminate the different processes responsible for the dynamics of the Congo River plume. Our methodology consists of (1) the setup of a three-dimensional regional hydrodynamic model over the west-central coast of Africa, (2) the validation of a realistically forced simulation, (3) the assessment of the seasonal variations of the Congo River plume, and (4) the determination of the processes responsible for the Congo River plume dynamics.

[5] The dominant properties of the plume are determined with (a) four sensitivity one year simulations where one of the main properties (wind, fresh water discharge, tides, and canyon) is removed and (b) two baseline simulations set up in a smaller domain where no forcing is imposed at the open boundaries.

[6] The model of the west-central coast of Africa forced by realistic fields is described in section 2. The results of the full and sensitivity simulations are analyzed in section 3, followed by a discussion and the conclusions in section 4.

2. Model Setup

2.1. Model Domain, Grid, Boundary Conditions and Numerical Configuration

[7] The simulations were carried out with version 451 (svn) of the Regional Ocean Modeling System (ROMS; http://www.myroms.org). ROMS is a free-surface, hydrostatic, split-explicit, primitive equation ocean model that uses stretched, terrain-following coordinates in the vertical and orthogonal curvilinear coordinates in the horizontal. ROMS model has been widely applied in river plume and inner-shelf circulation studies [*MacCready and Geyer*, 2001; *Hetland*, 2005; *Warneret al.*, 2005; *Choi and Wilkin*, 2007; *Chérubin and Richardson*, 2007]. A summary of the computational algorithms used in the model can be found in *Shchepetkin and McWilliams* [2005] and *Warner et al.* [2005].

[8] In our study, the model of the west-central coast of Africa (see Figure 1a) is on a regular Cartesian grid with a horizontal resolution of approximately 7 km, two coastal walls on the northern and the eastern sides, and two open boundaries. The domain includes most of the west-central coast of Africa (which in the model is covering an ocean surface of approximately 3.2×10^6 km^2) and is represented by a 298×234 grid point mesh. Realistic geometry and bathymetry (Global Topography v14.1; *Smith and Sandwell* [1997]) were used with a minimum depth set up at 5 m and a maximum ocean depth at 5500 m. The main bathymetric feature of our study area is the Congo canyon (800 km long and 1200 m deep, see Figure 1b). The model has 35 layers in the vertically stretched terrain-following ROMS σ coordinate, with resolution focused near the surface and the bottom (σ coordinate parameters used are $h_c = 400$ m, $\theta_s = 10.0$, and

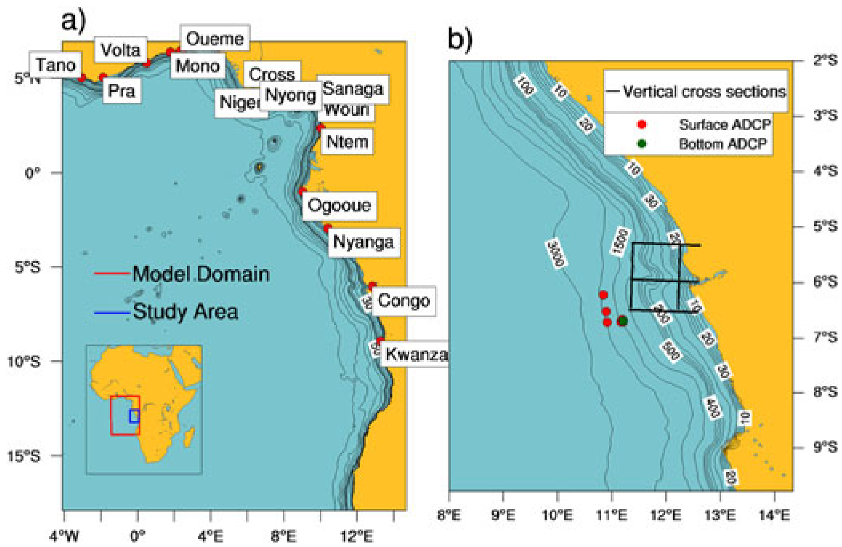

Figure 1. (a) Bottom topography of the model domain (m) and name of the rivers forcing the model. (b) Bottom topography of the study area (m). Dots are representing the location of the wind sensor and surface ADCP measurements (in red) and of the bottom ADCP measurements (in green) used for the validation of the model in section 2b and 3a. Black solid lines are the vertical cross sections where, along 12.1°E and 6.06°S, the salinity profiles and the momentum balance are presented (sections 3b, 3c, and 3d) and, along 5.4°S, 6.6°S and 11.24°E, the fresh water transport is calculated (sections 3c and 3d).

$\theta_s = 2.0$). The estimate of the vertical gradients is done with conservative splines.

[9] At the open boundary, the Flather conditions [*Flather*, 1976] are used for the barotropic velocity with the corresponding Chapman conditions [*Chapman*, 1985] for the surface elevation. The baroclinic velocities and the tracers are imposed with the Orlanski radiation conditions [*Orlanski*, 1976] modified by *Raymond and Kuo* [1984] to account for the horizontal propagation. In addition, an eight-grid point wide nudging relaxation zone with a folding time of 3–30 days is used to relax the baroclinic structure (temperature, salinity, and velocity) toward the fields provided by the ocean climatology [*Marchesiello et al.*, 2001]. A sponge area is also defined in such a way that the horizontal viscosity is four times bigger at the boundary than seven grid points away from it.

[10] At the coastal wall, the normal velocity is zero and a no-slip condition is used for the tangential velocity. There is no flow normal to the coastline. At the bottom, momentum is dissipated by a quadratic bottom drag coefficient ($Cd = 10^{-3}$). Salt and heat fluxes normal to the bottom and to the coast are set to zero.

[11] The numerical configuration uses the Multidimensional Positive Definite Advection Transport Algorithm (MPDATA) [*Smolarkiewicz*, 1983; *Smolarkiewicz*, 1984; *Smolarkiewicz and Clark*, 1986; *Smolarkiewicz and Grabowski*, 1990] for tracers with a grid-scaled horizontal diffusivity equivalent to $1.0\,\mathrm{m^2\,s^{-1}}$ for a $1\,\mathrm{km^2}$ grid cell. A third-order upwind scheme is used for horizontal momentum advection, with a Smagorinsky-like viscosity applied. The turbulence closure scheme used to calculate vertical mixing is GLS *gen* described by *Umlauf and Burchard* [2003]. *Warner et al.* [2005] demonstrated that this scheme is suitable for estuarine and plume modeling as they obtain similar salinity distributions for the three following schemes: $k-\epsilon$, $k-w$, and *gen*. The background, or minimum, mixing is defined as $10^{-5}\,\mathrm{m^2\,s^{-1}}$ for momentum and $10^{-6}\,\mathrm{m^2\,s^{-1}}$ for tracers. Both shear and stratification are averaged horizontally before mixing rates are calculated.

2.2. Tidal, Atmospheric, and Ocean Forcing

[12] The tidal forcing is added to the open boundaries and imposed on the elevation and the barotropic velocities. It is derived from the 11 tidal harmonics (the four main semi-diurnal components: M_2, S_2, N_2, and K_2; the four main diurnal components: K_1, O_1, P_1, and Q_1; and three overtide components: M_4, MS_4, and MN_4) extracted from the 1/12° resolution Atlantic Ocean Atlas solution (OSU Tidal Data Inversion) [*Egbert et al.*, 2004; *Egbert and Erofeeva*, 2002]. The analysis of the different harmonics provided by the OSU model revealed that within our study area the tidal forcing is dominated by the semi-diurnal component M_2. In the vicinity of the Congo River mouth (6°S, 12.15°E at approximately 85 m depth), the tidal range is approximately 1.6 m during the spring and 0.8 m during the neap associated with tidal currents below $0.06\,\mathrm{m\,s^{-1}}$.

[13] The air-sea heat and momentum fluxes are calculated by bulk formulas [*Fairall et al.*, 1996] using the model sea surface temperature, the 2 m air temperature, the sea level pressure, the 2 m relative humidity, the precipitations, the total cloud cover, the downward shortwave and longwave radiations, and the 10 m winds from European Centre for Medium-Range Weather Forecasts (ECMWF) ERA-Interim re-analysis climatology [*Dee et al.*, 2011]. The spatial resolution of these six-hourly ERA-I fields is 0.75°. The turbulent fluxes for wind, heat, and moisture are computed using Monin-Obukhov similarity theory such as *Liu et al.* [1979] and the net longwave radiation is derived using the *Berliand and Berliand* [1952] formula.

[14] During a 1 year period from May 2005 to May 2006, within our study area (see surface ADCP locations in Figure 1b), meteorological data were collected by the *Woods Hole Group* [2006] for BP Exploration (Angola) Ltd. The wind measurements have a significant gap from late July until early December 2005 (see Figure 2a) and mostly reflect conditions that occur during the austral summer (rainy season). During the period of the measurements, persistent southerly winds (with a fairly constant speed of approximately $5\,\mathrm{m\,s^{-1}}$) were recorded (see Figure 2a).

[15] The atmospheric circulation, in our study area, is controlled by a low-pressure system over Africa moving from the 15°W meridian toward equatorial regions during the austral summer (October to March) and toward the Sahara during the austral winter (April to September). *Schneider et al.* [1995] explained that the 16°S parallel is approximately the northern boundary of the zonally directed trade wind field. This field is influenced by the low-pressure system, which is weakening and changing to meridionally directed trade winds near the continent.

[16] Figure 2 and Table 1 summarize the statistical analysis performed on the wind speed and wind direction difference between the ERA-I wind fields and the recorded data. The mean speed bias of $-1.1\,\mathrm{m\,s^{-1}}$ and the minimum bias of $-6\,\mathrm{m\,s^{-1}}$ clearly highlight the underestimation (approximately 22%; see Figure 2b) of the wind speed by the ERA-I re-analysis data. Nevertheless, the correlation coefficient of 0.7 and the quantile-quantile (or Q-Q) plot (see Figure 2b)

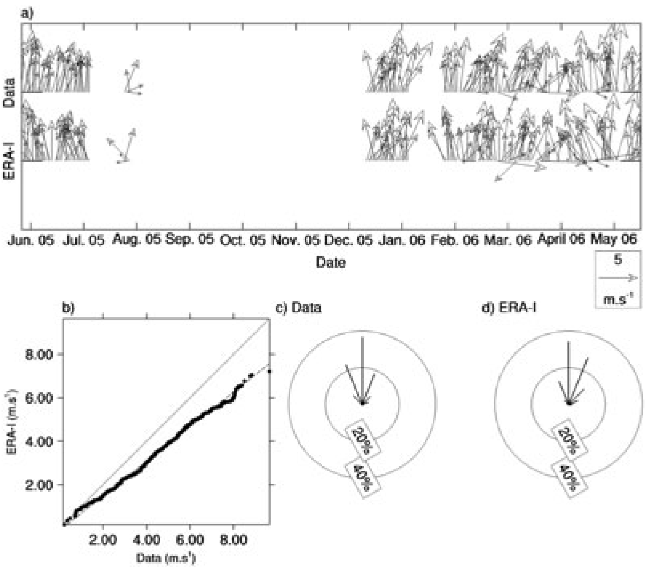

Figure 2. Comparison of the wind data from the buoy with the ERA-I reanalysis fields for the period of the measurements (May 2005 to May 2006): (a) Time series of wind vectors, (b) Q-Q plot of wind speed, and (c and d) wind roses.

show a good agreement between the ERA-I wind speed and the measurements. The standard deviation of 34.5° and the 12.5° of bias for the direction imply that on average the ERA-I winds are shifted eastward (see wind roses in Figures 2c and 2d). This eastward shift of the wind is quite unexpected as the study area is supposed to be dominated by the meridional winds.

[17] However, given the difficulty to reproduce the exact wind field at one location, the ERA-I winds are considered to be satisfactory.

[18] The eastern equatorial Atlantic, where the model was set up, is a complex region which was extensively studied [*Mittelstaedt*, 1991; *Baev and Polonsky*, 1991; *Richardson and Walsh*, 1986; *Arnault*, 1987]. The well-known surface currents in the equatorial region are the eastward-flowing North Equatorial Counter Current (NECC), the westward-flowing South Equatorial Current (SEC), and the eastward-flowing South Equatorial Counter Current (SECC). South of the equator, a branch of the SECC, the Angola Current (AC) flowing south along the Angola coast joins the northward-flowing Benguela Coastal Current (BCC) at the Angola-Benguela front near 16°S-14°S [*Wedepohl et al.*, 2000]. North of the front, in our region of interest, the BCC can be detected as a narrow subsurface tongue up to 5°S [*Van Bennekom and Berger*, 1984].

[19] The southward-flowing Angola current is a fast (0.5 m s^{-1} in the section nearest the African coast), narrow, and stable flow that covers both the shelf regions and the continental slope [*Moroshkin et al.*, 1970].

[20] In the vicinity of our study area, the Angola dome—a cyclonic eddy doming of the thermocline centered near 10°S and 9°E [*Lass et al.*, 2000], is also an important feature. The Angola dome, which disappears during the austral winter [*Mazeika*, 1967], is a cold water dome generated by a local maximum of Ekman suction [*McClain and Firestone*, 1993]; its shape depends on the intensity and horizontal shear of the southeasterly trade wind [*Signorini et al.*, 1999]. *Mazeika* [1967] attributes the drop of salinity of 0.3–0.5 psu within the Angola dome to the vertical mixing of low-salinity Congo River water from the surface layer.

[21] In order to realistically reproduce the complex ocean circulation, the 1/12° resolution HYbrid Coordinate Ocean Model (HYCOM) global daily analysis data are applied not only at the open boundaries and over the nudging area but also as the initial condition of the model. As highlighted by *Schiller et al.* [2011] the downscaling of larger-scale coarser models and, more precisely, the nesting to a data-assimilative model is a desirable approach to ensure proper shelf-to-offshore interactions. The HYCOM simulation employs the Navy Coupled Data Assimilation (NCODA) system [*Cummings*, 2005], which is an oceanographic version of the multivariate optimum interpolation technique commonly employed in atmospheric forecasting systems. The NCODA system assimilates satellite altimetry track-by-track and sea surface temperature (SST) directly from orbital data using model forecasts as the first guess [*Schiller et al.*, 2011].

Table 1. Statistical Summary of the Wind Speed Difference Between ERA-I and the Wind Sensor Data

	Speed (m s^{-1})	Direction (°)
Mean bias	−1.1	12
Maximum bias	4.0	178
Minimum bias	−6.0	−170
Root-mean-square difference	1.7	
Correlation coefficient (no unit)	0.7	0.4
Standard deviation	1.3	34

2.3. River Input

[22] Within the domain, 15 rivers are represented as active boundary conditions where temperature, fresh water, and outflow are specified with at least six source points along the channel of each river (see Figure 1a). The momentum flux is distributed uniformly over the first 3 m of the water column (i.e., the discharge is 18 times bigger at the surface than 3 m deeper), but in practice the added momentum is rapidly dissipated in the narrow model estuaries represented by two cells. The estuary of the Congo River is represented in the model with a 5 m deep, approximately 56 km long, and 14 km wide channel (i.e., 8×2 grid cells), and the discharge of the river is specified at 12 source points. For all the rivers, a salinity of nearly zero and the monthly skin temperature extracted from the ERA-I reanalysis fields [*Dee et al.*, 2011] are imposed at the sources.

[23] The monthly mean discharge of most of the rivers (Tano, Pra, and Volta Rivers in Ghana; Mono and Oueme Rivers in Benin; Cross River in Nigeria; Wouri, Sanaga, Nyong, and Ntem Rivers in Cameroon; and Ogooue and Nyanga Rivers in Gabon) was extracted from the RivDIS v1.1 database [*Vörösmarty et al.*, 1998]. However, the monthly mean discharge of the Niger Delta and the Kwanza River was estimated respectively from the Niger-HYCOS project Bulletin of January 2008 (http://www.whycos.org/fck_editor/upload/File/Niger-HYCOS/) and from the GEMS/GLORI database [1995].

[24] For the Congo River, more than 100 years of monthly mean discharge collected at Brazzaville between 1902 and 2005 were provided by the BEI ERE (http://hmf.enseeiht.fr/travaux/CD0809/bei/beiere/groupe5/node/53) in collaboration with the University of Brazzaville. The statistical analysis of this data set, carried out by *Laraque et al.* [2001], leads to the definition of three main phases during the XXth century: a "stable phase" between 1902 and 1959 with a mean discharge of 41,677 $m^3 s^{-1}$, a "wet phase" in the 1960s with a 15% increase of the discharge (47,978 $m^3 s^{-1}$), and a "dry phase" between 1980 and 1995 with a 10% drop of the discharge (40 600 $m^3 s^{-1}$). The analysis of the most recent data collected between 1995 and 2005 reveals that the Congo River is still in a "dry phase" and, in our study, the seasonal variations of the Congo River discharge were thus derived from the monthly data averaged between 1980 and 2005. Four characteristic periods can be clearly defined from the monthly Congo River discharge averaged over the "dry phase" (see Figure 3): (1) a first rise season occurring between October and January with a maximum discharge of 55,200 $m^3 s^{-1}$ in December, (2) a first fall season marked by a minimum discharge of 34,000 $m^3 s^{-1}$ in February–March, (3) a second rise season reaching 36,700 $m^3 s^{-1}$ between April and June, and (4) a second fall season between July and September with a minimum discharge of 30,100 $m^3 s^{-1}$ in August. For our numerical simulations, we were particularly interested in the most recent measurements of the monthly mean discharges and more particularly in years 2004 and 2005 (see Figure 3). During

these 2 years, the monthly discharges are slightly lower than the averaged values over the "dry period," which tends to confirm the downward trend of the Congo River discharge over the past 25 years [*Laraque et al.*, 2001]. Moreover, in 2004, only two characteristic periods can be distinguished: a rise season October–March and a fall season April–August. The decomposition of the Congo River discharge in four seasons is therefore not a permanent feature. However, the maximum and the minimum discharges always occur during December–January and July–August, respectively. After 2005, when the measurements stopped, the monthly discharge of the Congo River was assumed to be constant in the model and equal to the monthly discharge recorded in 2005.

[25] The four seasons used in this study are defined by the Congo River discharge variability: October to January (ONDJ), February and March (FM), April to June (AMJ), and July to September (JAS).

2.4. Model Simulations

[26] Over the entire domain, we have performed a realistic simulation from 1 January 2005 to 31 December 2008 (used as a "Control" run) and four sensitivity simulations where one property was turned off at a time: "No Wind" run, "No Canyon" run, "No Tide" run, and "Salt water discharge" run. The "Salt water discharge" simulation, forced by the discharge from the Congo River (realistic momentum flux) with ambient salinity (no salt flux), was set up with the aim of ascertaining the impact of the fresh water on the circulation and used to obtain the background salinity over the entire domain.

[27] In order to carry out a process-orientated study, a baseline model—which domain only covers the study area—was set up with the same grid resolution, bathymetry, river discharges, and numerical settings than the model of the west-central coast of Africa used for the "Control" run and the sensitivity simulations. The baseline model includes one coastal wall on the eastern side and three open boundaries where no forcing was imposed (no flow, no tracer, and no tide). Only three main rivers were taken into account in the baseline model: the Nyanga River (approximately 3°S of latitude), the Congo River (approximately 6°S of latitude), and the Kwanza River (approximately 9°S of latitude). The simulations were initiated with no flow and a flat sea surface. The initial tracer distribution was uniform background salinity of 35 psu, with vertical temperature stratification typical of the Congo River mouth during austral summer (a 10 m homogeneous mixed layer above exponential stratification with a 30 m decay scale ranging from 25°C at the surface to 8°C at the bottom).

Figure 3. Monthly mean discharge of the Congo River at Brazzaville for the period of the simulation (2005), for the spin-up period (2004), and as an average over the dry period (1980–2005).

[28] We carried out two process-orientated simulations: a "Baseline" run only forced with the realistic river discharges and a "Baseline Wind" run with the atmospheric forcing added.

[29] To understand the Congo River plume dynamics, the seasonal variations of the plume were the first to be accessed. As the most recent data of the Congo River discharge in our possession were taken in 2005, it was decided to undertake the simulations for the "Control" run, the sensitivity simulations, and the "Baseline Wind" run during this year. The "Baseline" simulation was run only during 40 days in order to avoid the generation of spurious currents resulting from the interaction of the fresh water plume with the open boundaries of the domain.

[30] For all the sensitivity simulations, a 1 year spin-up run was set up in 2004 in order to let the model adjust to both the initial condition (interpolated vertically from the global HYCOM archives provided in Cartesian *z* level into the ROMS σ coordinates) and the various changes imposed on the scenarios. Table 2 summarizes the initial, the forcing, and the boundary conditions used in the numerical experiments undertaken in this study.

3. Results

3.1. Validation of the Model

3.1.1. Currents

[31] Two different data sets of Acoustic Doppler Current Profiler (ADCP) measurements were provided by BP Exploration (Angola) Ltd. in order to validate the model in the vicinity of our study area.

[32] During the period from May 2005 to May 2006, the *Woods Hole Group* [2006] collected current data at six well sites located offshore from the Congo River mouth (see red dots in Figure 1b). A near-surface data set (high frequency ADCP) was obtained between 8 and 28 m of depth with a 1 m resolution and a deeper data set (low frequency ADCP) was collected between 73 and 841 m with a 24 m resolution (Table 3). The ADCP data quality assessment and quality control revealed a higher quality data for the low frequency ADCP observations compared to the upper layer high frequency data set. The 1 year time series of measurements were obtained by combining together the records and the depths of the two ADCPs at the six different stations.

[33] Between June 2007 and May 2008, near-bottom currents at a location named Farfield (green dot in Figure 1b) were recorded between 881 and 1393 m of depth with a 16 m resolution low frequency ADCP. However, no data quality assessment was provided with this data set and only 25% of the data were valid. The daily time series of eastward and northward surface velocities for both the ADCP data (see Figures 4a and 4b) and the ROMS model (see Figures 4c and 4d) are presented between 8 and 841 m of depth.

[34] Due to the frequent gaps in the measurements, a harmonic or spectral analysis could not be performed. However, a review of the time series carried out by the *Woods Hole Group* [2006] revealed three major time scales of variability: (1) a low frequency variability of 0.15 m s^{-1} amplitude and a 3–6 month period, (2) inertial oscillations of 0.05 m s^{-1} and approximately a 4 day period, and (3) tidal

Table 2. Summary of the Initial, Forcing, and Boundary Conditions Used in the Model Simulations

Runs	Initial Condition	Forcing	Boundary Conditions
		Sensitivity Study—Realistic 1 year Runs Setup in 2005	
Control	Provided by a 1 year spin-up run setup in 2004	Fresh water river discharges Atmospheric and tidal forcing	1/12° global HYCOM archives
No wind		$0\,m\,s^{-1}$ winds	
Salt water discharge		35 psu river salinity	
No tide		No tidal forcing	
No canyon		Depth of the canyon manually changed	
		Process-Orientated Study	
Baseline	35 psu uniform salinity Vertical profile of temperature: from 25°C at the surface to 8°C at the bottom	Fresh water river discharges	No forcing imposed
Baseline wind	No current	Fresh water river discharges atmospheric forcing	

Table 3. Coordinates of the Well Locations Where the ADCP Measurements Were Taken and Dates of Data Collection

Well	Period of Collection	Depth (m)	Latitude	Longitude
Astraea-1	23 May to 01Jul 2005	1495	6°49′39.610″S	11°06′22.027″E
Hebe-1	21 May to 08 Sep 2005	2009	6°38′58.421″S	10°47′22.871″E
Plutao-2	15 Sep to 25 Oct 2005	2033	6°20′57.259″S	10°43′22.275″E
Mercurio-1	04 Nov to 07 Dec 2005	1592	6°49′48.654″S	11°03′52.677″E
Urano-1	11 Dec 2005 to 22 Mar 2006	1938	6°50′42.907″S	10°48′52.750″E
Astraea-2	23 Mar to 11 May 2006	1465	6°47′06.249″S	11°05′19.354″E

variations ($0.1\,m\,s^{-1}$) dominated by semi-diurnal tides. The low frequency variations are generally reproduced by the model (see Figure 4) for the eastward and the northward velocities. The strong northward events of June and December 2005 are particularly well simulated even if the current speed is slightly underestimated in the upper mixed layer (approximately the first 20 m of depth). The strong northward surface velocities recorded between February and April 2006 are underestimated in the model. This may be explained by the combination of the low quality of the measurements and/or the inaccuracy of the ERA-I wind forcing (underestimate of the wind speed and bias in direction).

[35] Concerning the highest frequency variations, the physics used within the ROMS model takes into account both the inertial oscillations and the tidal variations. The inertial currents are caused by rapid changes of wind at the sea surface, and they may not be well represented due to the inaccuracy of the ERA-I wind forcing.

[36] Figure 5 shows the mean bias and the standard deviation between the model results and the ADCP data for both the speed and the direction. The results obtained with the three ADCPs at different times and locations and for various depths are surprisingly consistent. However, a change of the mean bias for both the speed and the direction can be seen

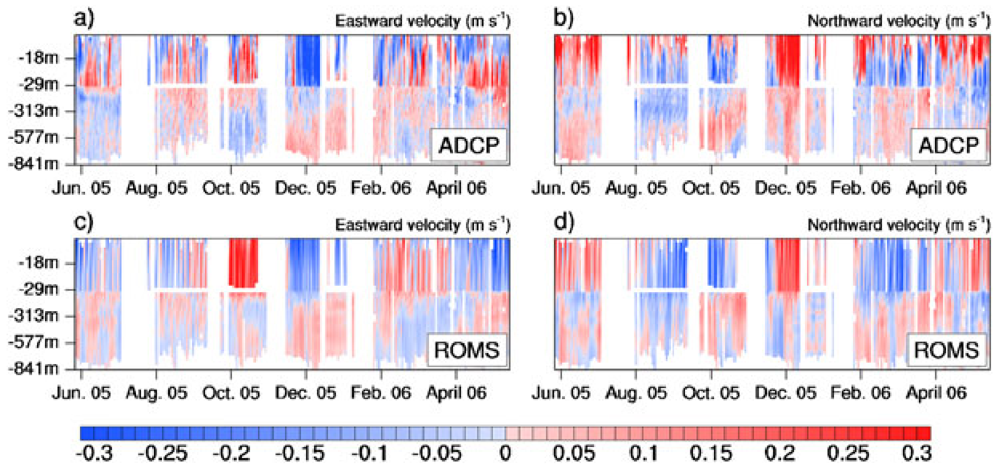

Figure 4. Eastward and northward velocity components of the combined time series of (a and b) the in situ surface measurements and of (c and d) the model results represented over the vertical for the entire period of the observations (May 2005 to May 2006). The vertical scale is defined with a regular interval between the bins of the two ADCPs. A 24× zoom is applied to the surface measurements between 8 and 29 m of depth.

between 26 and 121 m (shade in light grey in Figure 5). It is caused by the combination of the data from the high frequency ADCP (8–29 m) with the low frequency ADCP (73–841 m) and probably shows that the first bins of the high frequency ADCP and/or the first bins of the downward-looking low frequency ADCP should be ignored. In the following analysis, these bins will not be taken into account.

[37] The highest bias in speed ($-0.05\,\mathrm{m\,s^{-1}}$) is reached between 9 and 14 m of depth (see Figure 5a) and is associated with the largest standard deviation ($>0.14\,\mathrm{m\,s^{-1}}$; see Figure 5b). On average, the underestimation of the current speed is about 25% which is similar to the underestimate of the wind speed by the ERA-I fields. As the thickness of the Congo River plume might be shallower than 10 m and disperses in the upper 10 m of water column, the underestimate of the wind and the upper 10 m surface velocities introduce a bias in the modeling of the dispersal of plume. Outside of the upper mixed layer (see Figures 5a and 5b), the mean bias and the standard deviation are fairly constant (respectively -0.015 and $0.04\,\mathrm{m\,s^{-1}}$) to 841 m of depth. Below 881 m of depth (see Figures 5e and 5f), the mean bias linearly increases from -0.015 to $0.01\,\mathrm{m\,s^{-1}}$, and the model is thus overestimating the speeds on the last 300 m of depth.

[38] Concerning the direction of the surface currents between 8 and 841 m of depth (see Figures 5c and 5d), the highest mean bias is found between 20 and 409 m of depth with an underestimation of the direction of 15° and the associated standard deviation is in average of 94°. For the bottom currents (see Figures 5g and 5h), the mean bias varies between $-6°$ and 6° and is associated with a standard deviation of 98°.

[39] The *Woods Hole Group* [2006] highlights that the area where the yearly long surface current observations were collected is located quite near the bifurcation point of the South Equatorial Counter Current (SECC). The measured flows outside of the upper mixed layer are indeed characterized by almost zero mean current velocities. It is in consequence a challenging area in terms of direction of the currents as the extension of the SECC may flow northward or southward (Angola Current) depending on the seasonally and inter-annual variability. Due to the 7 km resolution of the model and the high spatial variability of the current direction in the area of the measurements, it is hard to reproduce the data measured at one station and the model may well described the overall physics of the area.

3.1.2. Sea Surface Temperature

[40] The model was compared against the Group for High Resolution Sea Surface Temperature (GHRSST) L4 Sea Surface Temperature (SST) analysis produced daily at the NOAA National Climatic Data Center. These data used optimal interpolation from AVHRR Pathfinder Version 5 data, AMSR-E, and in situ ship and buoy observations. The Optimum Interpolation 1/4° analysis [*Reynolds et al.*, 2002; *Reynolds et al*., 2007] is a daily average SST that is bias adjusted using a spatially smoothed 7 day in situ SST average. In order to perform the comparison between the model results and the satellite data, the SST has been linearly interpolated on each node of the ROMS domain.

[41] The seasonal climatology of the temperature bias between the model results and the satellite data—derived from the 4 years of the realistic run and not presented in this study—shows that within our study area the ROMS model always overestimates the SST. This bias is not related to the HYCOM SST forcing (where remote sensing data are assimilated) and is either caused by the atmospheric forcing or the bulk formulae used in the ROMS model.

[42] In order to check the overall estimation of the SST by the ROMS model, statistical analysis was performed on daily time series of temperature extracting at each node of the model. Table 4 lists the results of the statistical analysis. With a 0.75 correlation coefficient of the residual (seasonal variations were subtracted) and a mean bias of 1.4°C, it can be estimated that the model is in general agreement with the GHRSST-NOAA satellite data.

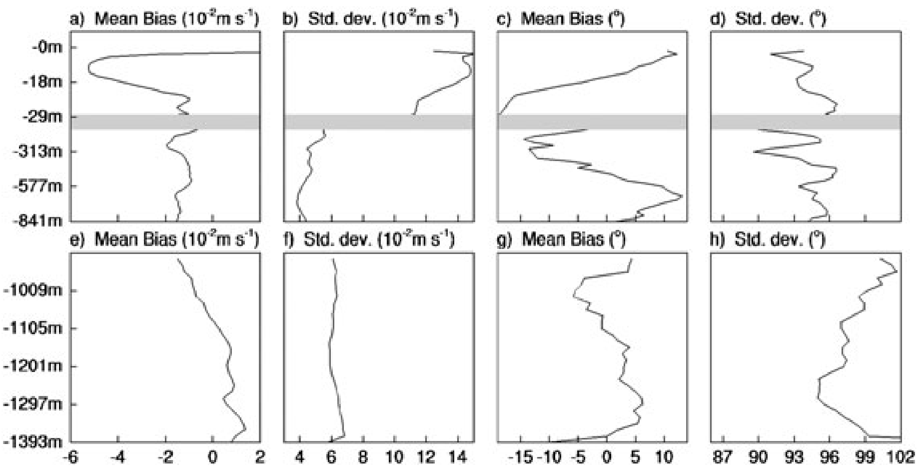

Figure 5. Statistical summary of the (a, b, e, and f) current speed and (c, d, g, and h) direction difference between the ROMS model and the ADCP data provided between 8 and 841 m of depth (May 2005 to May 2006) and between 871 and 1393 m of depth (May 2007 to June 2008). The vertical scale is defined with a regular interval between the bins of the three ADCPs. A 24× zoom is applied to the surface measurements between 8 and 29m depth. The light grey shaded area represents the bins ignored during the statistical analysis.

3.1.3. Sea Surface Salinity

[43] The ocean color merged data sets, developed within the NASA REASON/MEaSUREs and ESA GlobColour projects [*Maritorena et al.*, 2010], and more particularly the colored detrital matter absorption (a_{cdm}) from the SeaWiFS, MODIS-AQUA, and MERIS ocean color missions for the 2002–2009 time period, were used in order to validate the seasonal variations of the Congo River plume. *Salisbury et al.* [2011] proved that salinity and a_{cdm} patterns were generally similar in the vicinity of the Amazon River plume although they generally tend to deviate at the more distal regions of the low-salinity plume. Given the lack of salinity measurements within the Congo River plume, a qualitative comparison between the a_{cdm} and the model results was undertaken.

[44] The seasonal climatology of the Sea Surface Salinity (SSS) of the ROMS model during 2005 was qualitatively compared against the a_{cdm} climatology between 2002 and 2009 (see Figures 6a–6d) and the HYCOM SSS during 2005 (see Figures 6e–6h). During the ONDJ and AMJ seasons, the isohalines from the ROMS model seem to be matching the pattern of the a_{cdm} climatology (see Figures 6a and 6c) and the 34 psu isohaline corresponds to a value of 0.5 m^{-1} of the a_{cdm}.

[45] During the FM season, the isohalines from the ROMS model are shifted north in comparison with the a_{cdm} pattern, but the westward extend of the 34 psu isohaline from the ROMS model and the 0.5 m^{-1} isoline from the a_{cdm} climatology is similar (see Figure 6b). During the JAS season, the ROMS model well reproduced the general pattern of the a_{cdm} climatology (see Figure 6d) but the 34 psu isohaline corresponds to a value of nearly 1 m^{-1} of the a_{cdm} which indicates that the western extend of the plume is probably underestimated by the model during this period. The a_{cdm} climatology and the distribution of the surface chlorophyll—highly affected by the local Ekman pumping [*Signorini et al.*, 1999], follow similar seasonal variations. Due to the coarse resolution of the ERA-I win field, the local Ekman pumping is not well represented in the ROMS model and is thus a potential source of the differences observed between the ROMS SSS and the a_{cdm} pattern.

[46] The comparison between the isohalines of the ROMS model and the HYCOM SSS (see Figures 6e–6h) clearly shows that the fresh water plume of the Congo River from HYCOM is underestimated: the 34 psu isohaline of HYCOM corresponds to the 27 psu isohaline of the ROMS model. As the ROMS and HYCOM grids have a similar resolution, this underestimation of the fresh water plume can be explained by the discharge of the Congo River and/or by the mixing scheme used in the model.

[47] In summary, the spatial distribution of ROMS salinity is similar to the pattern of the a_{cdm} except during JAS season, and the ROMS model seems to reproduce the surface salinity features of the plume more accurately than

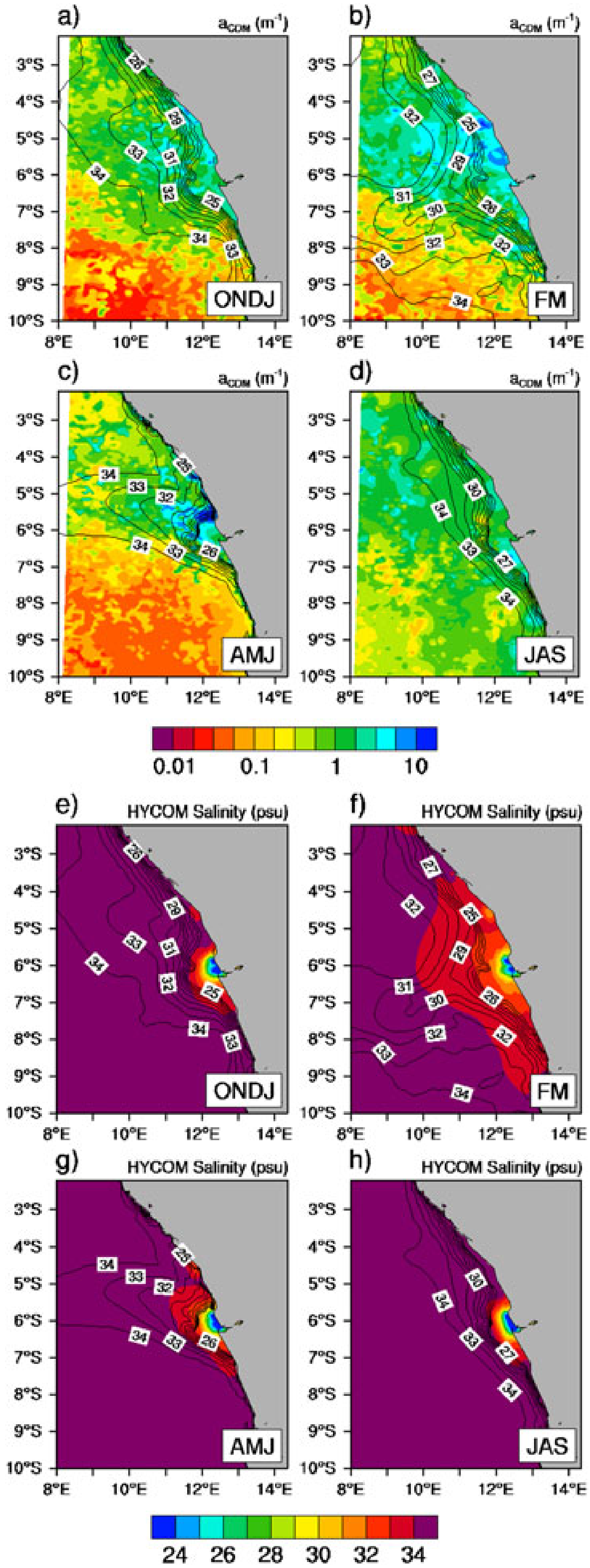

Figure 6. Seasonal variations of the ROMS model sea surface salinity (1 psu isohalines interval between 25 and 34 psu) superimposed to the (a–d) CDM absorption coefficient and the (e–h) HYCOM sea surface salinity.

Table 4. Statistical Summary of the Sea Surface Temperature (SST in °C) Difference Between the ROMS Model and the GHRSST-NOAA Satellite Data

	Temperature
Mean bias	1.4
Root mean square difference	1.9
Correlation coefficient of the residual (no unit)	0.75
Standard deviation	1.2

HYCOM. However, this purely qualitative study must be confirmed by a more quantitative approach including the calculation of the synthetic salinity and in situ measurements.

3.1.4. General Circulation

[48] A comparison between the HYCOM and ROMS model surface currents (see Figure 7) was undertaken in order to (1) estimate the capacity of HYCOM to reproduce the complex surface circulation of the West African Atlantic Ocean, (2) compare the general circulation of the ROMS model with HYCOM, and (3) identify the main sources of the differences between the output of the two models.

[49] For all the seasons, the westward-flowing South Equatorial Current (SEC) and the eastward-flowing North Equatorial Counter Current (NECC) are well reproduced by both models (see Figures 7a–7d for the ROMS model and Figures 7e–7h for HYCOM). However, the eastward-flowing South Equatorial Counter Current (SECC) can only be seen in HYCOM during the ONDJ season (see Figure 7e). Despite the absence of the SECC, both models clearly reproduce the Angola Current (AC) flowing south along the Angola coast and the Angola-Benguela front located at the southern boundary of the domain. None of the models reproduce the Angola Dome: neither the drop of temperature (about 8°C) nor the cyclonic gyre characteristic of the thermal dome is modeled near 10°S and 9°E. However, the Guinea Dome—another thermal dome—is well reproduced by both models during the AMJ and JAS seasons (see Figures 7c and 7d for the ROMS model and Figures 7g and 7h for HYCOM).

[50] The main differences between the two models are (1) the increased intensity and size of the westward-flowing SEC in the ROMS model and (2) the opposite direction of the nearshore drift north of the Congo mouth: northward in the ROMS model and southward in HYCOM. The nearshore northward drift (in ROMS) is probably driven by the Congo River discharge which is apparently underestimated in HYCOM (see Figure 6).

[51] Concerning the SEC, the main difference between the two models—apart from the numerical settings—is the atmospheric forcing. More precisely, the wind stress and the surface heat flux are some important drivers of the surface ocean circulation and the use of different atmospheric re-analysis fields in the two models can partially explain the differences between the ROMS and HYCOM surface currents. The good agreement of the ERA-I wind fields with the measurements done by the *Woods Hole Group* [2006] validates the use of these atmospheric re-analysis fields in the vicinity of the Congo mouth but not over the all domain.

[52] We took advantage of the 2 years of surface and bottom ADCP data provided by BP and of the available SST and a_{cdm} satellite data in order to carefully assess the performance of the model over the area of interest. Despite the difficulty of the model to reproduce all the dynamical features of the upper mixed layer (which can be attributed to the atmospheric forcing, the distribution of the sigma levels, and/or the mixing scheme used), reasonable results were generally obtained. Moreover the seasonal variations of the model salinity derived for 2005 is in good agreement with the a_{cdm} climatology. The comparison with the HYCOM surface salinity and currents reveals some important differences between the two models: (1) the underestimate by HYCOM of the horizontal dispersion of the Congo River plume and (2) the strong influence of both the atmospheric forcing and the Congo River discharge on the strength and direction of respectively the SEC and the nearshore drift in the vicinity of the plume. As the aim of the study is to understand the processes driving the Congo River plume by switching off

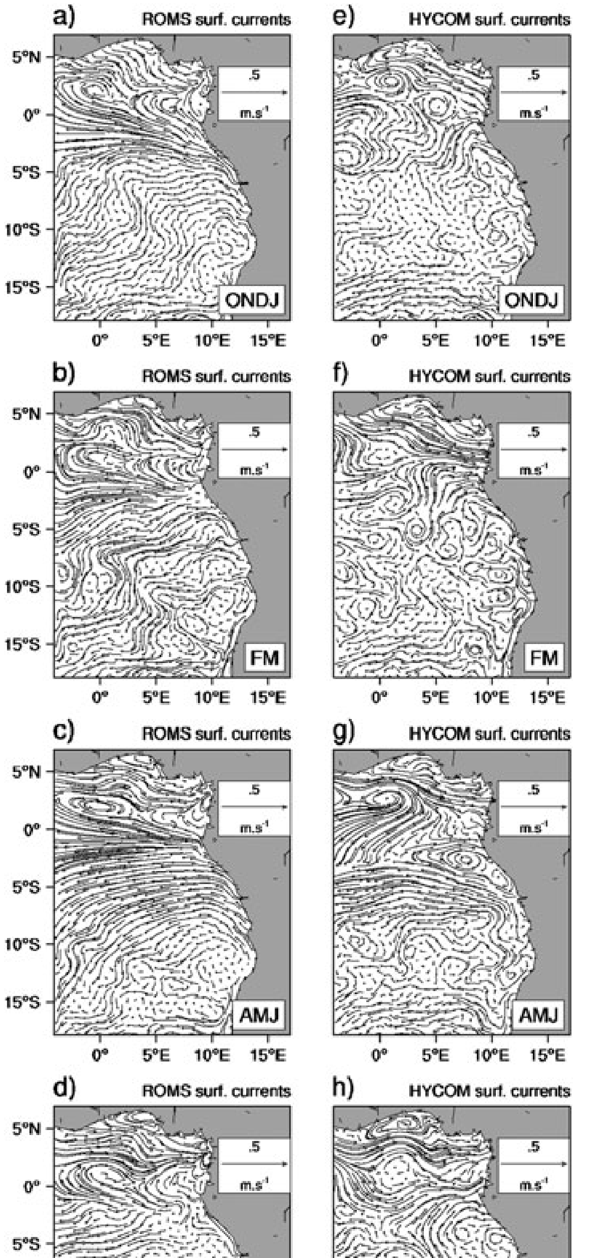

Figure 7. Seasonal variations of the sea surface currents—comparison between (a–d) ROMS and (e–h) HYCOM results.

one property at the time and comparing the results given by the different runs, the validation of the model is considered to be satisfactory even if the model has a near-surface intrinsic bias.

3.2. Horizontal Structure of the Congo River Plume

3.2.1. Plume Characterization

[53] The methods used to characterize the Congo River plume are comparable to that used by *Schiller et al.* [2011] for the Mississippi River, by *Choi and Wilkin* [2007] for the Hudson River, and by *Hetland* [2005]. However, this study focuses on the seasonal variations of the plume dynamics instead of the description of some particular short-term events.

[54] In this study, the surface plume pattern is described by the salinity and currents at the first sigma level (near surface), the fresh water thickness, and the upper layer Froude number. The fresh water thickness (δ_{fw}) represents the equivalent depth of fresh water and is mathematically described by

$$\delta_{fw} = \int_{-h}^{n} \frac{S_b - S(z)}{S_b} dz, \tag{1}$$

where S_b is the background salinity associated with the background density ρ_b, $S(z)$ is the depth-dependent diluted salinity due to the river discharge, η is the sea level, and h is the bottom depth. The run with ambient salt discharge from the Congo River was used in order to obtain the background salinity over the study area.

[55] The upper layer thickness (δ_{ul}) is defined by *Hetland* [2005] as the depth where the salinity is equal to the average between the minimum value ($S_{\min}$) and the maximum value ($S_{\max}$) of salinity. The upper layer phase speed (C_{ul}), the upper layer velocity (u_{ul}), and the upper layer Froude number (F_{ul}) are hence defined by

$$C_{ul} = \sqrt{g\delta_{ul} \frac{\rho_b - \int_{-\delta_{ul}}^{\eta} \rho(z)dz}{\rho_b}} \tag{2}$$

$$u_{ul} = \int_{-\delta_{ul}}^{n} |u(z)|dz, \tag{3}$$

$$F_{ul} = \frac{u_{ul}}{c_{ul}}, \tag{4}$$

[56] where g is gravitational acceleration, $\rho(z)$ is the depth-dependent density, and $\mathbf{u}(z)$ is the depth-dependent flow speed.

[57] The upper layer Froude number discriminates the near-field river plume region which is characterized by Froude numbers greater than 1 (supercritical outflow) from the subcritical far-field plume region [*Wright and Coleman* [1971]; *Chao* [1988]; *Hetland* [2005]. The main drivers of the near-field region are the buoyancy and the tides in close association with the geomorphology of the river estuary while the far-field dynamics are mostly controlled by the wind forcing and the geostrophic circulation.

3.2.2. Seasonal Variations of the Far-Field Plume Orientation

[58] The analysis of the "Control" run results reveals that the Congo River plume exhibits strong variations in shape over the year (see Figures 8.1–8.3 and 9). The westward extension and the fresh water thickness of the plume—associated with a low Froude number $F_{ul} \ll 1$ (see Figure 8.3) and thus particularly subject to the influence of the wind and the ocean circulation—present a wide range of variations over the different seasons. The 33 psu salinity contour reaches 8°E during February–March (see Figure 8.1b) with a fresh water thickness, δ_{fw}, above 1 m for most of the plume (see Figure 8.2b), about 9.5°E during the ONDJ and AMJ seasons (see Figures 8.1a and 8.1c) associated with $\delta_{fw} =$ 0.65 m (see Figures 8.2a and 8.2c), and only 11°E during the JAS season (see Figure 8.1d) with $\delta_{fw} < 0.6$ m (see Figure 8.2d). The maximum fresh water surface area defined as the area where the surface salinity is below 33 psu (Figure 9) is also reached during the FM season with a value of about 6×10^{11} m^2 which is twice the mean value for the rest of the year. The increase of the fresh water surface area of the plume in January followed by the rapid drop in early April is not correlated with the maximum river discharge reached during December–January. This spread is confirmed by *Eisma and Kalf* [1984] who describe the Congo River outflow as a thin layer of low-salinity water that can be traced as far as 8°E. *Signorini et al.* [1999] show that the westward extension of the chlorophyll is highly dependent on the period of the year and that the maximum westward extension of the surface chlorophyll is found in February–March while the minimum occurs between September and December.

[59] The other noticeable and fairly permanent feature is the northward extension of the Congo River plume with the presence of strong longshore currents (0.25 m s^{-1}) and low salinity (<24 psu) along the coast of Gabon (Figure 8.1). The fresh water thickness of this northward plume varies between 0.3 m during the austral winter (AMJ and JAS)—when the northward extension of the plume varies between 100 and 300 km—and 0.7 m during the austral summer (ONDJ and FM) when the plume reaches 2°S of latitude (i.e., northward extension of 450 km). It would have been expected that the plume turns left (southward) as result of the Coriolis force. The Coriolis parameter (f) at the latitude of our study area is about -0.15×10^{-4} s^{-1} and the derived Kelvin number (K_e which is the ratio of Coriolis force to density effects [*Garvine*, 1995]) associated with the Congo River plume is approximately -0.4. The Coriolis force is thus not the main driver of the Congo River plume dynamics. *Eisma and Kalf* [1984], who also notice this northward extension, explain it by the influence of the northward-flowing Benguela Coastal Current (BCC) over the shelf.

[60] The study of the seasonal surface variations of the Congo River plume thus reveals two major properties: (1) the persistent extension of the plume toward north and (2) the large extent toward west during FM season.

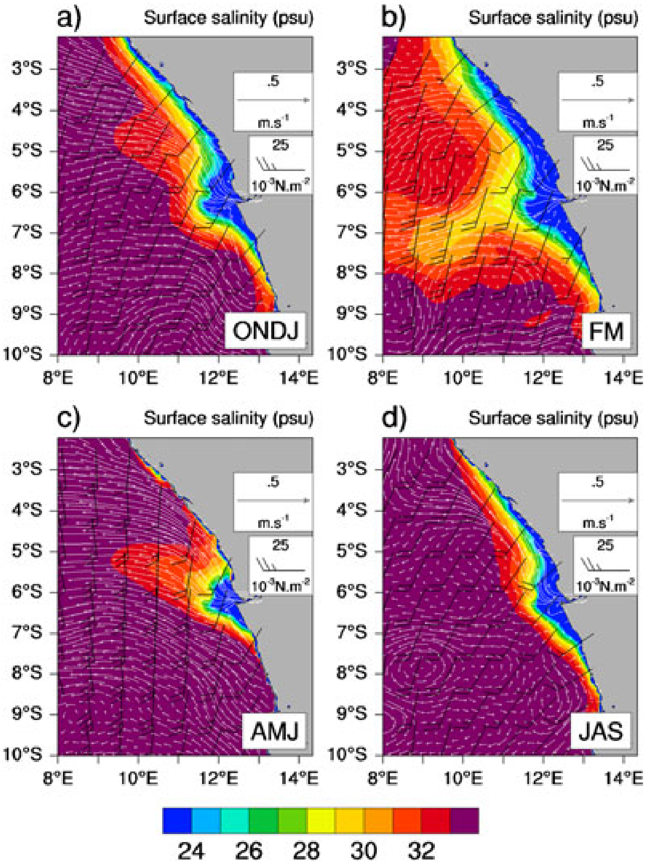

Figure 8.1. "Control" run—seasonal variations of the sea surface salinity, currents (white vectors), and wind stress (black barbs) for (a) ONDJ, (b) FM, (c) AMJ, and (d) JAS.

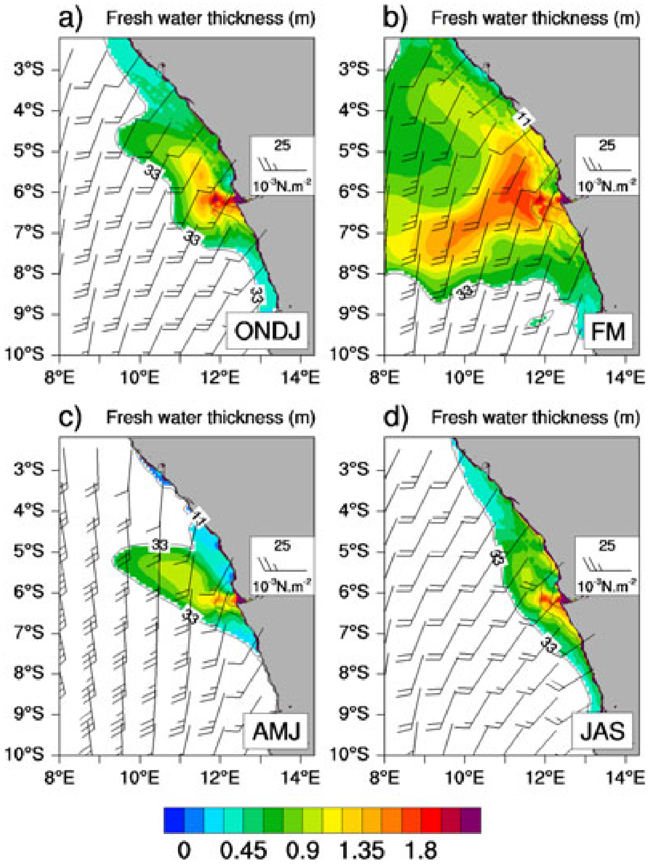

Figure 8.2. "Control" run—seasonal variations of the fresh water thickness, isohalines (black solid lines) and wind stress (black barbs) for (a) ONDJ, (b) FM, (c) AMJ, and (d) JAS.

3.2.3. Effects of the Geomorphology

[61] The "Baseline" run only forced by the bathymetry and the river discharges was used (1) to provide assurance that the model correctly represents a "typical" river plume and (2) to characterize the effects of the geomorphology on the orientation of the plume. Figures 10.1 and 10.2 show the properties of the plume for the "Baseline" simulation.

[62] After 10 days of simulation (see Figure 10.1a), the Congo River plume follows a typical behavior as described by *Chao* [1988]: a bulge has formed just downstream—in the Kelvin wave sense—of the estuarine outflow, with a recirculating gyre and only a portion of the freshwater introduced continues southward as a buoyancy-driven downstream coastal current ($0.5\,\mathrm{m\,s^{-1}}$). In this scenario, only a third of the freshwater input into the domain is carried away by the coastal current. The freshwater thus accumulates within the bulge which expands (100 km wide; see Figure 10.1a) and thickens ($1.2\,\mathrm{m} < \delta_{fw} < 1.5\,\mathrm{m}$; see Figure 10.2a). The three regions of the plume (estuarine, near-field, and far-field) are clearly discernible (see Figure 10.1a) but, due to the huge amount of fresh water input in the domain by the Congo River discharge, their salinity ranges are noticeably lower than in the test case described by *Hetland* [2005]. The estuarine outflow surface salinity is nearly 1 psu, the upper layer salinity leaving the estuary and forming the near-field area ranges from 1 to 11 psu, and the water of the far-field area has an upper layer salinity of approximately 25 psu. However, even after 10 days of simulations (see Figure 10.1a), the Congo River plume presents two unique features: (1) a strong northwestward drift ($>0.5\,\mathrm{m\,s^{-1}}$) following the Congo River canyon and (2) an upstream (northward) coastal current ($0.2\,\mathrm{m\,s^{-1}}$) in the vicinity of the Congo River mouth. Due to the Coriolis effect, both of these flows turn southwestward and join the recirculating gyre. The far-field water recirculates within the bulge, creating a thick, homogeneous mass of water. The freshwater thickness associated with the northwestward drift is increasing during the period of the simulation: $1.2\,\mathrm{m} < \delta_{fw} < 1.5\,\mathrm{m}$ after 10 days (see Figure 10.2a), $1.5\,\mathrm{m} \ll \delta_{fw} < 1.9\,\mathrm{m}$ after 20 days (see Figure 10.2b), and $\delta_{fw} > 2\,\mathrm{m}$ for the rest of the simulation (see Figures 10.2c and 10.2d). In consequence, a certain amount of fresh water is trapped within the Congo River canyon area. Concerning the other rivers of the baseline domain, the Nyanga River (north of the Congo River—approximately 3°S of latitude) and the Kwanza River (south of the Congo River—approximately 9°S of latitude), they follow a typical behavior (recirculating gyre and downstream coastal current) with no northward current formed.

[63] After 20 days of simulation, the upstream coastal current generated by the Congo River discharge has increased in intensity and reached $0.5\,\mathrm{m\,s^{-1}}$ (see Figure 10.1b). This flow has also extended north, along the Gabon coast, to approximately 4°S of latitude and nearly joined the

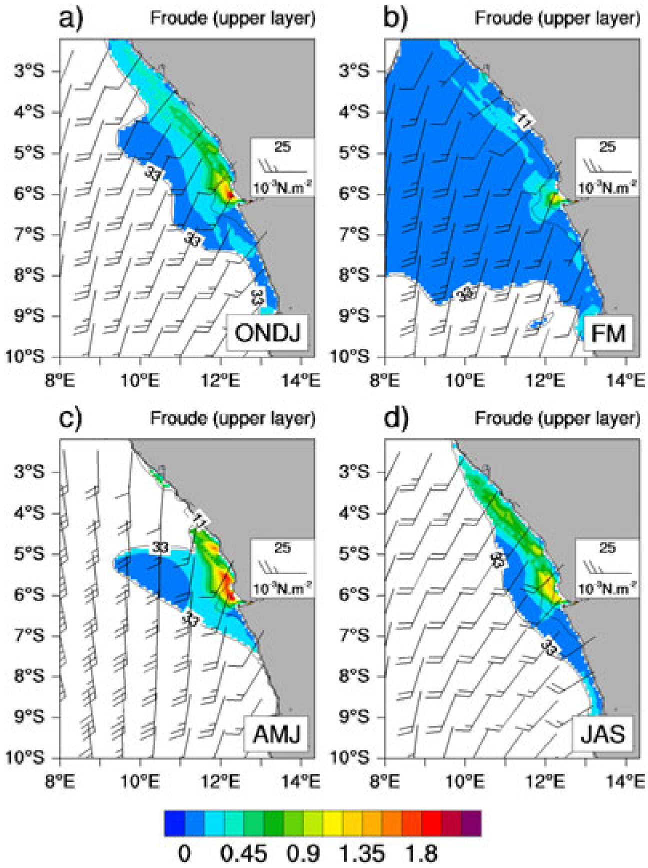

Figure 8.3. "Control" run—seasonal variations of the Froude number, isohalines (black solid lines) and wind stress (black barbs) for (a) ONDJ, (b) FM, (c) AMJ, and (d) JAS.

Nyanga River downstream flow (which has extended south). Due to the Coriolis effect, the upstream flow tends to turn southwestward in order to join the bulge area. A branch of northwestward drift following the Congo canyon turns north and feeds the northward flow while the other branch still feeds the bulge area. The downstream coastal flow is wider (about 50 km) and has extended to the southern boundary of the model. The fresh water thickness (δ_{fw}) associated with this downstream flow is about 1.2 m while the one associated with the upstream flow is approximately 0.4 m (see Figure 10.2b). The downstream flow thus remains the main driver of the transport of fresh water away from the Congo River bulge.

[64] After 30 days of simulation (see Figures 10.1c and 10.2c), the Congo River upstream flow has joined the bulge

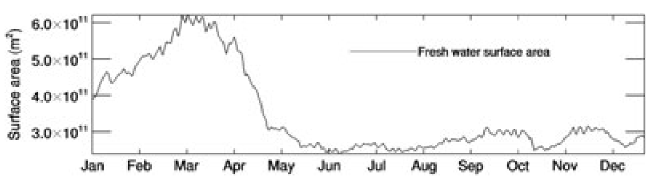

Figure 9. "Control" run—time series of the fresh water surface area of the Congo plume defined as the area with a surface salinity below 33 psu.

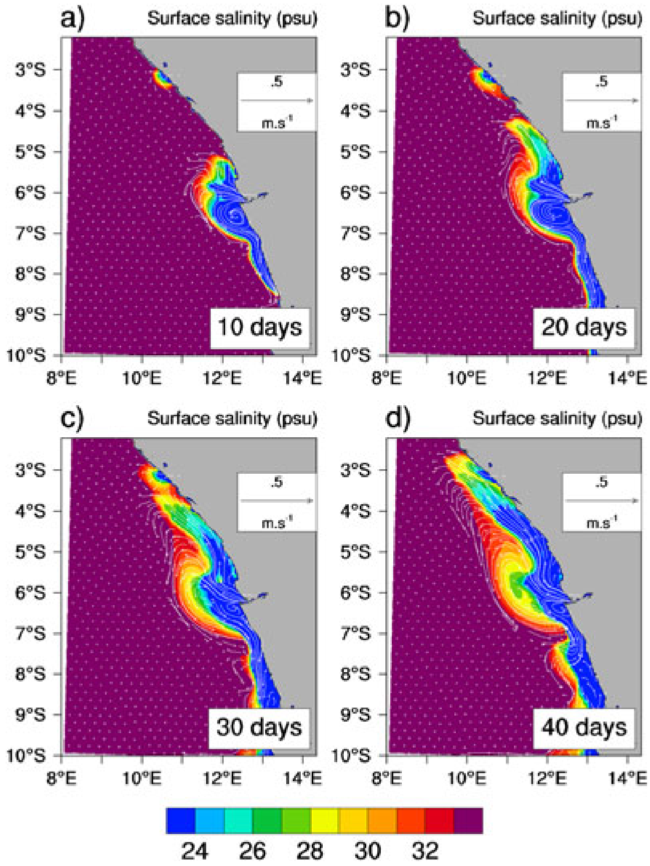

Figure 10.1. "Baseline" run—variations of the sea surface salinity and currents (white vectors) for (a) 10, (b) 20, (c) 30, and (d) 40 days.

of the Nyanga River and its fresh water thickness has increased, $\delta_{fw} = 0.6–0.8$ m. The Coriolis effect seems to be weaker than the buoyancy effect as only a fifth of the northward flow turns southwestward. The width and the fresh water thickness of the downstream coastal flow are still increasing (80 km and 1.5 m, respectively) but the intensity of the flow remains constant (about 0.5 m s^{-1}). At approximately 8.5°S of latitude, where the isobaths and the coastline have a deviation of 90°, an anticyclonic eddy is formed within the downstream flow and the fresh water is trapped ($\delta_{fw} = 1.8$ m).

[65] After 40 days of simulation (see Figures 10.1d and 10.2d), the Congo River upstream flow has nearly reached the northern boundary of the domain and reaches a maximal fresh water thickness (δ_{fw}) of 1.2 m with an average value of 0.9 m. The Nyanga River bulge has totally disappeared and the river plume is pushed northward by the Congo River upstream flow. The anticyclonic eddy formed within the downstream flow has increased and spreads between 8°S and 9°S of latitude where the fresh water cumulates ($\delta_{fw} > 1.8$ m). In consequence, although the upstream current is growing, the downstream flow remains the main driver of the transport of fresh water away from the bulge area. South of the Congo River mouth, at the edge of the recirculating gyre, this fresh water eddy pushes the downstream flow which first deviates westward before turning southward with a 90° angle.

[66] Summarizing the above analysis, the "Baseline" simulation—only forced by the bathymetry and the river

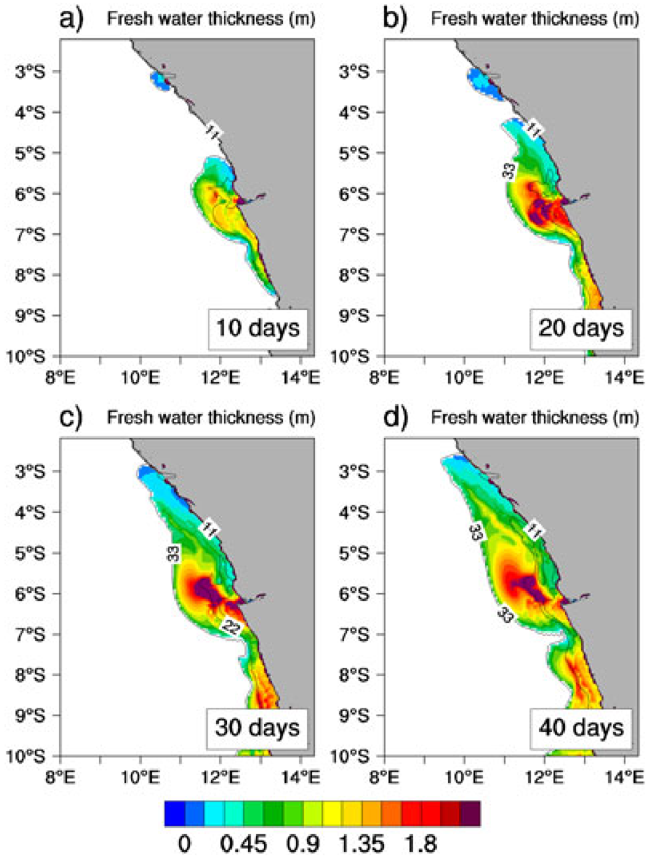

Figure 10.2. "Baseline" run—variations of the fresh water thickness and isohalines (black solid lines) for (a) 10, (b) 20, (c) 30, and (d) 40 days.

discharges—clearly highlights the strong effects of the geomorphology on the Congo River plume buoyancy-driven dynamics: (1) presence of a strong northwestward drift following the Congo River canyon where the fresh water is accumulating, (2) generation of a strong upstream coastal current growing in time (increase in intensity, northward expansion, and accumulation of fresh water), and (3) formation of an anticyclonic fresh water eddy within the downstream flow. The hypothesis of *Eisma and Kalf* [1984]—who explained the Congo River upstream coastal current by the influence of the northward-flowing Benguela Coastal Current (BCC) over the shelf—is at least incomplete as the unique geomorphology of the Congo River estuary has been proven to be a strong driver of the buoyancy-driven northward deflection of the Congo River plume.

3.2.4. Effects of the Wind

[67] In order to understand the seasonal effects of the wind on the horizontal plume structure and far-field dynamics, the atmospheric forcing (wind stress and air-sea fluxes derived from the ERA-I fields) was added to the baseline model and the model was run over the same year as the "Control" run.

[68] The seasonal variations of the river plume dynamics for this "Baseline Wind" simulation are presented on the surface in Figure 11.

Southward Extension of the Plume

[69] A thin southward extension of the Congo River plume is still generated in the "Baseline Wind" run: during the ONDJ and JAS seasons, the branch is less than 10 km wide (see Figures 11a and 11d) and associated with a fresh water thickness of about 0.4 m (see Figures11e and 11h) but reaches 50 km during the FM season with $\delta_{fw} = 0.8$ m. However, during the AMJ season (see Figures 11c and 11g) the southward branch totally disappears. During the ONDJ and JAS seasons (see Figures 11a and 11d), downstream of the Congo mouth, the surface currents are weak ($<0.05\,\mathrm{m\,s^{-1}}$) but northward. The southward extension of the plume is clearly not driven by the surface currents. Moreover, the southward branch is associated with small but not negligible upper layer Froude numbers (about 0.3; see Figures 11i–11l) and the flow must be driven by the density effects. During the FM season (see Figure 11b), a bulge is formed and a downstream coastal current is generated ($>0.25\,\mathrm{m\,s^{-1}}$). However, due to the action of the wind, the downstream flow is partially turning northwestward in order to join the wind-driven general circulation. The behavior of the plume during the FM season, similar to the behavior of the "Baseline" run plume, can be explained by the weakness of the winds blowing along the coast during this period: the seasonal averaged wind stress is indeed lower than $9 \times 10^{-3}\,\mathrm{N\,m^{-2}}$ during the FM season (see Figure 11b) while, during the ONDJ and AMJ seasons (see Figures 11a and 11c), it is always greater than $13 \times 10^{-3}\,\mathrm{N\,m^{-2}}$ and reaches up to $21 \times 10^{-3}\,\mathrm{N\,m^{-2}}$ during the JAS season (see Figure 11d).

Northward Extension of the Plume

[70] The northward extension of the plume is separated in two distinct branches: (1) a thick northwestward drift following the Congo River canyon—associated with 1.4–2 m fresh water thickness (see Figures 11e–11h) and $0.5\,\mathrm{m\,s^{-1}}$ currents (see Figures 11a–11d)—turning northward and joining (2) a thinner upstream coastal current flowing northward along the Gabon coast with an intensity of about $0.5\,\mathrm{m\,s^{-1}}$ for the ONDJ, AMJ, and JAS seasons (see Figures 11a, 11c, and 11d) and less than $0.1\,\mathrm{m\,s^{-1}}$ for the FM season (see Figure 11b) when the seasonal averaged wind stress is weak along the coast. The fresh water thickness associated with the northward flow is about 1.3 m in the vicinity of the Congo River mouth and 0.9 m further north for the ONDJ, FM, and JAS seasons (see Figures 11e, 11f, and 11h) but only 0.3 m for the AMJ season (see Figure 11g). The upper layer Froude number associated with the northward coastal current is about 0.4 for the ONDJ and FM seasons (see Figures 11i and 11j) but reaches up to 1 during the AMJ and JAS seasons (see Figures 11k and 11l). In consequence, although the wind remains the main driver of the northward extension of the plume, the buoyancy still plays an important role (as described in section 3.2.3).

Westward Extension of the Plume

[71] In contrast with what was expected in the "Control" run, the westward extension of the plume does not occur during the FM season (see Figure 8.1b) but during the AMJ season (see Figure 11c). The westward extension of the plume, associated with low upper layer Froude number ($F_{ul} < 0.3$; see Figure 11k), is clearly driven by the wind and more precisely by the wind direction.

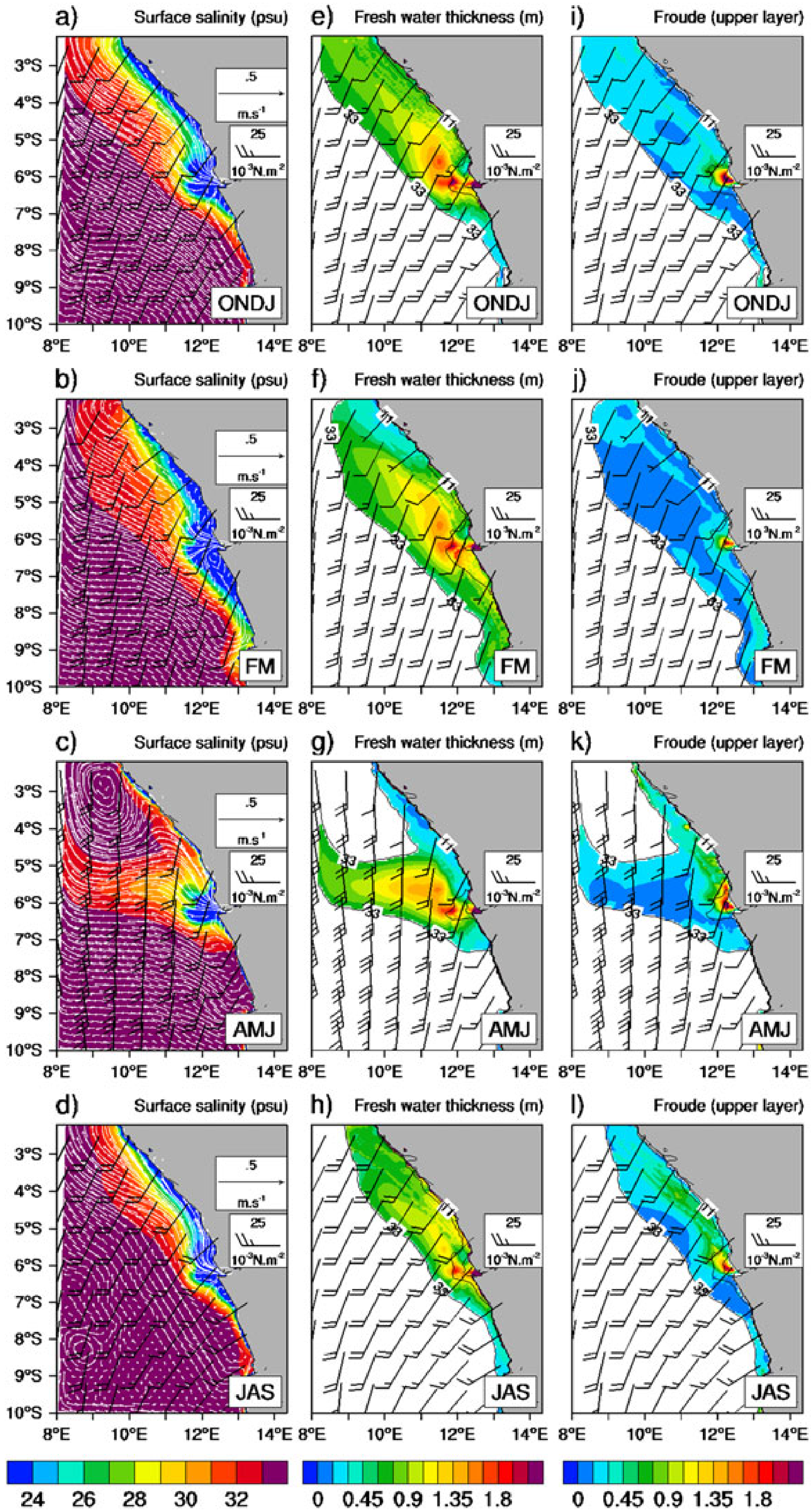

Figure 11. "Baseline Wind" run—seasonal variations of the (a–d) sea surface salinity and currents, (e–h) fresh water thickness, and (i–l) Froude number.

During the AMJ season, the averaged wind stress is indeed northward or northwestward in most of the domain (see Figure 11c). In consequence, due to the Coriolis effect, the surface current of the Ekman spiral is directed westward and the general circulation is driven by a westward flow (see Figure 11c). The westward flow is driving the entire model except in the northern boundary of the domain where a gyre is formed. This gyre may be caused by some spurious boundary effects and is not necessarily related to the wind effects. During the other seasons (see Figures 11a, 11b, and 11d), the averaged wind stress is northeastward and the general circulation is driven by a northward flow following the coast. The westward extend of the Congo River plume, during the AMJ season (see Figure 11g), is thick ($0.9\,\mathrm{m} < \delta_{fw}$ $1.8\,\mathrm{m}$ with an averaged value of 1.35 m) and has a westward extend of more than 500 km (the 33 psu isohaline reaches 8°E of longitude).

[72] In summary, by comparison with the results obtained with the "Baseline" run (see Figures 10.1 and 10.2)—where a third of the Congo River fresh water plume was carried away by the downstream coastal current—the major effects of the wind are (1) to reinforce the upstream coastal current which becomes the main driver of the transport of fresh water away from the Congo River mouth (in case of northeastward winds), (2) to weaken the downstream coastal current, (3) to avoid the formation of the bulge (except during the FM season when the wind is too weak), and (4) to generate a thick westward extension of the plume in case of northward winds (such as during the AMJ season). This "Baseline Wind" run also discards the wind as the main factor of the westward extension of the plume during the FM season (see "Control" run) and the general circulation seems to be the only factor left to explain it.

3.2.5. Effects of the Ocean Circulation

[73] With the aim of understanding the effects of the ocean circulation on the far-field plume dynamics, the model was run over the same year as the control run but (1) with an ambient salt discharge from the Congo River and (2) with a wind stress equal to zero (the other air-sea fluxes are still taken into account).

General Circulation Versus Buoyancy- and Wind-Driven Effects

[74] The run with ambient salt discharge from the Congo River was set up in order to discriminate the effects of the general circulation from the buoyancy- and the wind-driven effects (see Figure 12). During the ONDJ and AMJ seasons (see Figures 12a and 12c), the circulation along the Angola and Gabon coast is driven by a 200 km northwestward drift of $0.2\,\mathrm{m\,s^{-1}}$ on average. The northwestward drift is influenced by the general circulation as the effect of the wind—shown in the "Baseline Wind" run—is purely westward for the AMJ season and northward for the ONDJ season. This westward deflection of the nearshore circulation is thus probably influenced by the westward-flowing South Equatorial Current. During the FM season (see Figure 12b), the circulation along the Gabon coast is dominated by a southeastward current of $0.08\,\mathrm{m\,s^{-1}}$ but a northwestward current ($0.15\,\mathrm{m\,s^{-1}}$) can be noticed off the Congo mouth; it extends over 150 km before joining the southwestward main flow at approximately 4°S. The southwestward main flow is purely driven by the general circulation as the wind effect, shown in the "Baseline Wind" run, and is weak nearshore and purely northward offshore. The southwestward flow seems to be related to the South Equatorial Current. The nearshore circulation, during the JAS season (see Figure 12d), consists of a southward current ($0.15\,\mathrm{m\,s^{-1}}$ in average) following the coast of Gabon and Angola. This southward flow is again clearly driven by the general circulation and probably by the southward branch of the Angola Current.

[75] In brief, during the AMJ season, the general circulation strongly affects the plume orientation with a northwestward direction instead of the purely westward direction imposed by the wind ("Baseline Wind" run) and the purely northward direction of the upstream buoyancy-driven coastal current ("Baseline" run). During the ONDJ season, the westward influence of the general circulation is relatively weak and only affects the area of the plume where the salinity is above 32 psu. During the FM season, the effect of the ambient circulation is drastic for the westward extension of the plume but the northward coastal current is driven by the buoyancy. During the JAS season, the nearshore circulation is southward and the buoyancy is the main driver of the nearshore northward plume extension.

Northward Extension of the Plume

[76] The seasonal variations of the river plume dynamics for the "No Wind" simulation are presented on the surface in Figure 13. The most noticeable difference between the

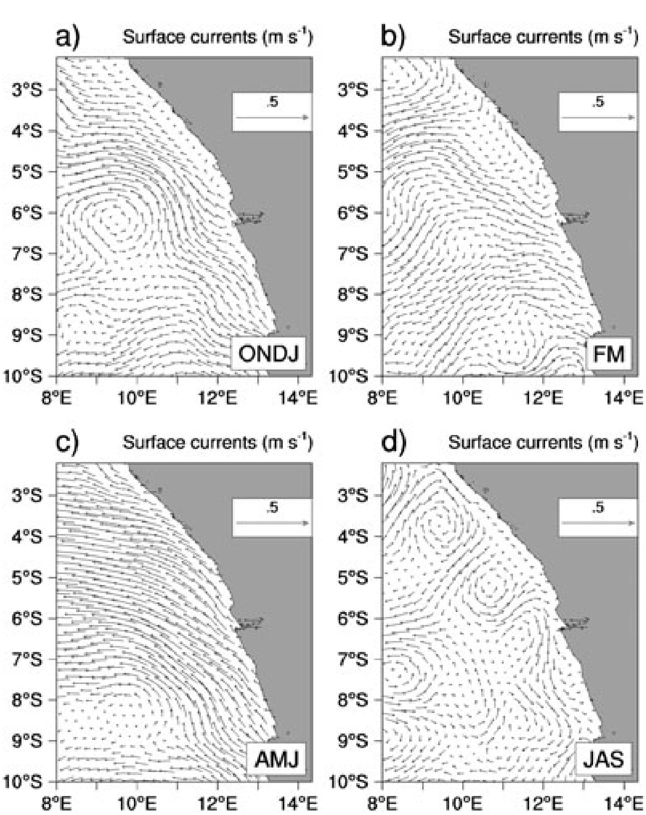

Figure 12. Seasonal variations of the surface currents for the simulation with ambient salt water discharge from the Congo River for (a) ONDJ, (b) FM, (c) AMJ, and (d) JAS.

"Control" run (Figures 8.1 and 8.2) and the results without wind is the split of the Congo River plume in two branches (similarly to the "Baseline" run after 40 days of simulation): (1) a thin northward nearshore branch with a fresh water thickness of about 0.4 m during ONDJ and AMJ seasons (see Figures 13e and 13g), 0.7 m during the FM season (see Figure 13f), and below 0.3 m during JAS season (see Figure 13h); and (2) a thicker southward nearshore branch associated with 1.2–1.5 m fresh water thickness and extended up to 400 km along the coast of Angola (see Figures 13e–13h). Both the northward and southward nearshore drifts have an intensity of about $0.25\,\mathrm{m\,s^{-1}}$ (see Figures 13a–13d). The southward branch is associated with small upper layer Froude numbers (below 0.3; see Figures 13i–13l), and the flow is thus driven by the density effects. Moreover, in the vicinity of the estuary, a bulge associated with a fresh water thickness greater than 2 m and an upper layer Froude number of about 1 is formed which is similar to the results found by *Hetland* [2005] and *Choi and Wilkin* [2007] for their runs without wind. However, during the ONDJ, FM, and AMJ seasons, the presence of the strong northward drift associated with Froude numbers of approximately 0.4 (see Figures 13i–13k) is not a typical feature. In this simulation, the wind is not the driver of this drift, however, as shown in the "Baseline" run, the geomorphology strongly affects the generation of the buoyancy-driven upstream coastal current.

[77] The relatively high values of the Froude number found outside of the bulge area ($F_{ul} \approx 0.45$ along the Gabon coast; see Figures 13i–13k) and of the thickness of the plume ($\delta_{fw} > 0.7$ m in the first 100 km; see Figures 13a–13c) noticed during the ONDJ, FM, and AMJ seasons can be mainly explained by the presence of the northwestward ambient flow for the ONDJ and AMJ seasons and the buoyancy effects for the FM season. During the JAS season (see Figures 13d and 13h), the northward extension of the plume is formed with denser water (salinity greater than 27 psu) than the rest of the year (salinity below 23 psu) and the plume is very thin ($\delta_{fw} < 0.2$ m). These results are similar to the "Baseline" run, the ocean is thus counterbalancing the effects of the wind and the buoyancy is the main driver during the JAS season.

Westward Extension of the Plume

[78] *Van Bennekom and Berger* [1984] associate the westward extension of the plume with the prevailing northward wind stress in the Angola Basin. However, for the "No Wind" simulation, the plume is still extending westward during the FM season when the 33 psu salinity contour reaches 9°E (see Figure 13b). Moreover, the "Baseline Wind" run clearly highlights that the effect of the wind during the FM season is purely northward. The fresh water thickness associated with the westward extension is above 0.9 m (see Figure 13f) and the upper layer Froude number is quasi null (see Figure 13j) which is similar to the results of the "Control" run. In the "No Wind" simulation, the westward extension of the plume is driven by a large and fast anticyclonic freshwater eddy (salinity below 30 psu and currents of $0.3\,\mathrm{m\,s^{-1}}$) located at 7.5°S between two cyclonic eddies associated with a salinity greater than 32 psu and currents below $0.2\,\mathrm{m\,s^{-1}}$ (Figure 13b). This complex circulation is similar to the one modeled in HYCOM (see Figure 7f) and thus seems related to the global ocean circulation. For both the "Control" run (see Figure 8.1b) and the run with the ambient salt discharge from the Congo River (see Figure 12b), strong southwestward ocean currents are modeled during the FM season. For the "No Wind" simulation, these southwestward ocean currents are probably less intense and the general circulation is more affected by the Coriolis and the density effects. This explains the dynamics of the "No Wind" simulation during the FM season: formation of eddies and reduced westward extension. Figures 8.1b and 12b also show the presence of a nearshore southward drift—probably generated by the southern branch of the Angola Current—which advects fresh water from the Nyanga River along the Gabon coast and joins the westward drift at 3°S. This fresh water input from the Nyanga River is combined with the Congo River discharge itself and is the explanation of the increase of the fresh water surface area of the Congo plume during the FM season (see Figure 9).

[79] The main drivers of the northward and westward extensions of the Congo River plume are summarized in Table 5.

3.3. Daily Variations of the Congo River Fresh Water Transport

[80] Another way to characterize the wind and the general circulation effects on the Congo River plume pathways is the calculation of the fresh water transport Q_{fw} across three sections that establish a closed region around the Congo River estuary (black solid lines for cross-sections along 5.4°S, 6.6°S, and 11.24°E; Figure 1b). The fresh water transport is derived as

$$Q_{\mathrm{fw}} = \int \int_{-h}^{n} \frac{S_b - S(x,z)}{S_b} V(x,z) dz dx, \qquad (5)$$

[81] where $V(x,z)$ is the horizontal velocity normal to the section and x is the horizontal distance along the section.

[82] The daily variations of the wind stress and of the fresh water transport across the three sections can be observed in Figure 14. Across the section located north of the Congo mouth (cross-section along 5.4°S; Figure 14b), the general pattern of the fresh water transport variations is similar for the "Control" run (in red), the "Baseline Wind" run (in green), and the "No Wind" run (in blue). However, the fresh water transport of the "No Wind" run is on average 25% lower than in the "Control" run. The high frequency variations of the "No Wind" transport along all the cross-sections depend on the heat flux (derived from the precipitation, evaporation, solar radiations, etc.) which are the dominant surface mechanisms in absence of wind but may also result from the nonlinearity of the flows. The values of the transport are generally positive which means that the fresh water transport is northward across this section. The presence of southward short events, associated with weak southerly winds or with strong northerly winds, can be noticed during the austral summer (FM and ONDJ). These events are more significant in the "Baseline Wind" run than in the "Control" run; they are thus mainly wind driven. The maximum of the northward fresh water transport is reached at the end of January for the "Control" run ($Q_{fw} = 13 \times 2000\,\mathrm{m^3\,s^{-1}}$), at the end of

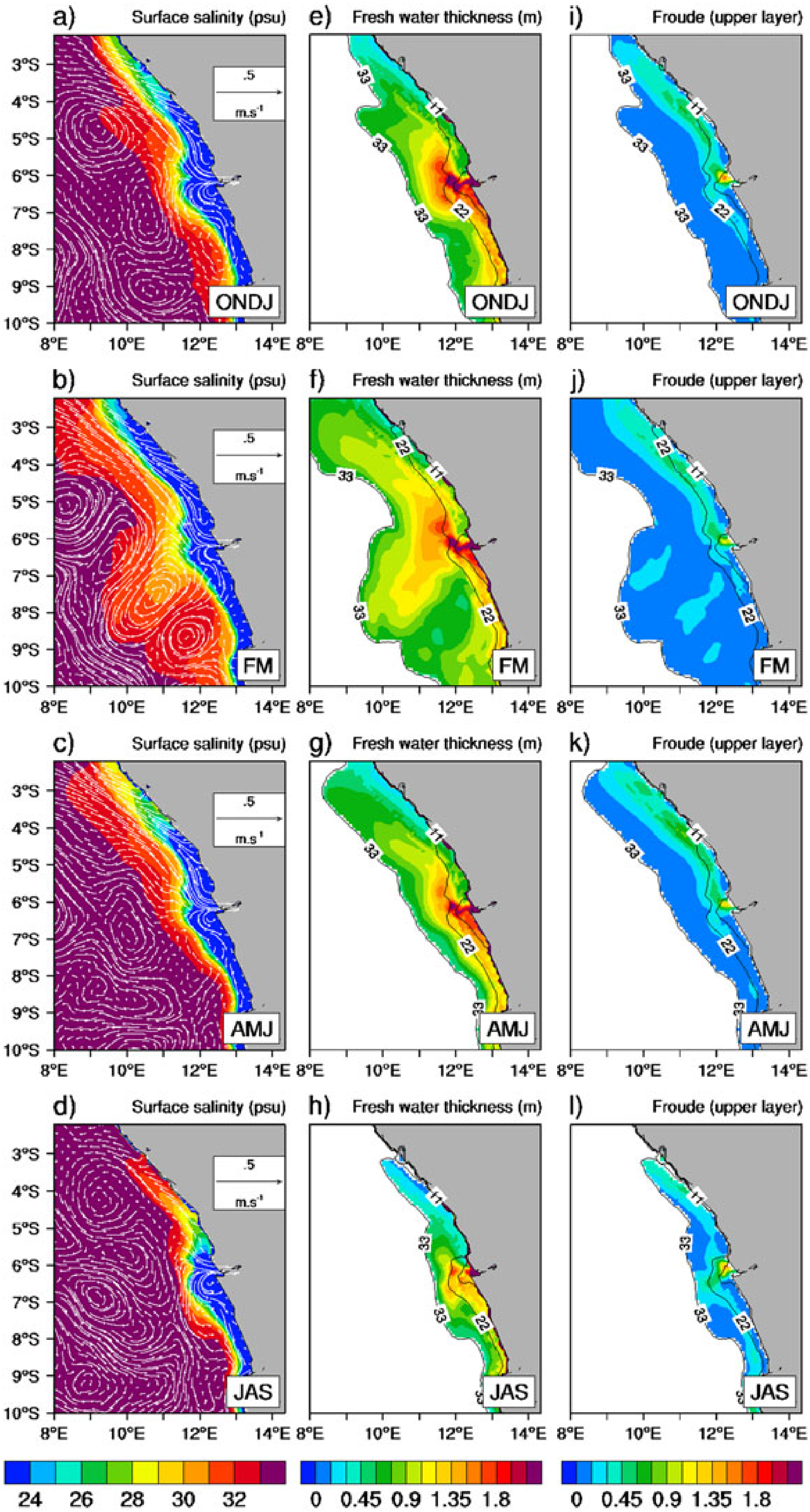

Figure 13. "No Wind" run—seasonal variations of the (a–d) sea surface salinity and currents, (e–h) fresh water thickness, and (i–l) Froude number.

Table 5. Summary of the Different Forcing Influencing the Seasonal Variations of the Horizontal Structure of the Congo River Plume[a]

	Buoyancy/Topography	Wind- driven effects	Ocean Circulation
		Northward Extension of the Congo River Plume	
ONDJ	Medium	High	Low
FM	Medium	Low (southward ocean circulation/northward wind)	
AMJ	Medium	Medium	Medium
JAS	Medium	Low (southward ocean circulation/northward wind)	
		Westward Extension of the Congo River Plume	
FM	None	None	High
AMJ	None	High	Medium

[a]High, medium, low, and none represent a qualitative estimate of the importance of each forcing.

November for the "No Wind" run ($Q_{fw} = 8 \times 6000\,\mathrm{m^3\,s^{-1}}$), and mid-February/start of November for the "Baseline Wind" run ($Q_{fw} = 9 \times 1000\,\mathrm{m^3\,s^{-1}}$). During the JAS season, when the maximum wind stress is reached, the transport for the "No Wind" run is quasi null on average while a northward transport is present in the control run ($Q_{fw} = 2 \times 8000\,\mathrm{m^3\,s^{-1}}$).

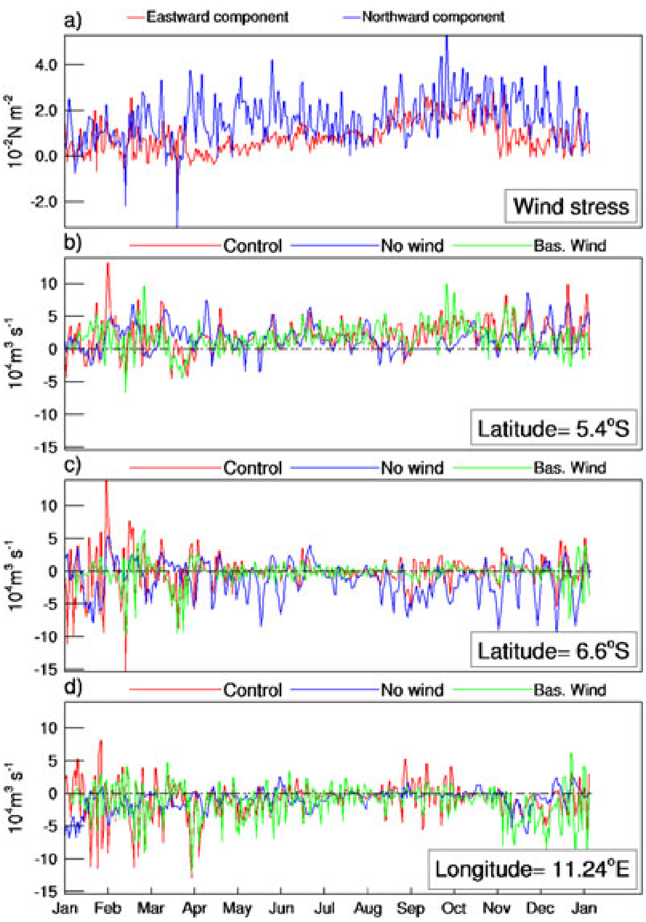

Figure 14. Time series of (a) wind stress components computed as spatial averages from area defined by 5.4°S, 6.6°S, and 11.24°E. Time series of the fresh water transport Q_{fw} across sections at (b) 5.4°S, (c) 6.6°S, and (d) 11.24°E. Positive/negative values represent eastward/westward transport across section at 11.24°E and northward/southward transport across sections at 5.4°S and 6.6°S.

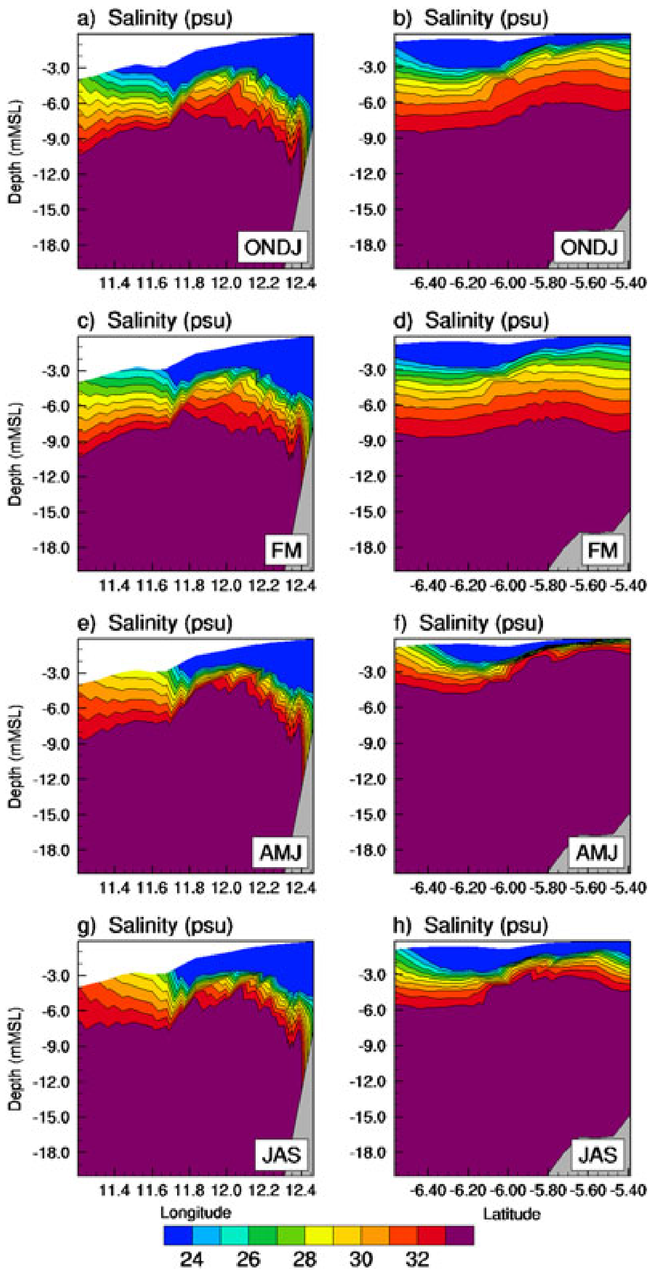

Figure 15. A "Control" run—seasonal variations of the salinity along the (a, c, e, and g) 6.06°S and (b, d, f, and h) 12.1°E cross-sections.

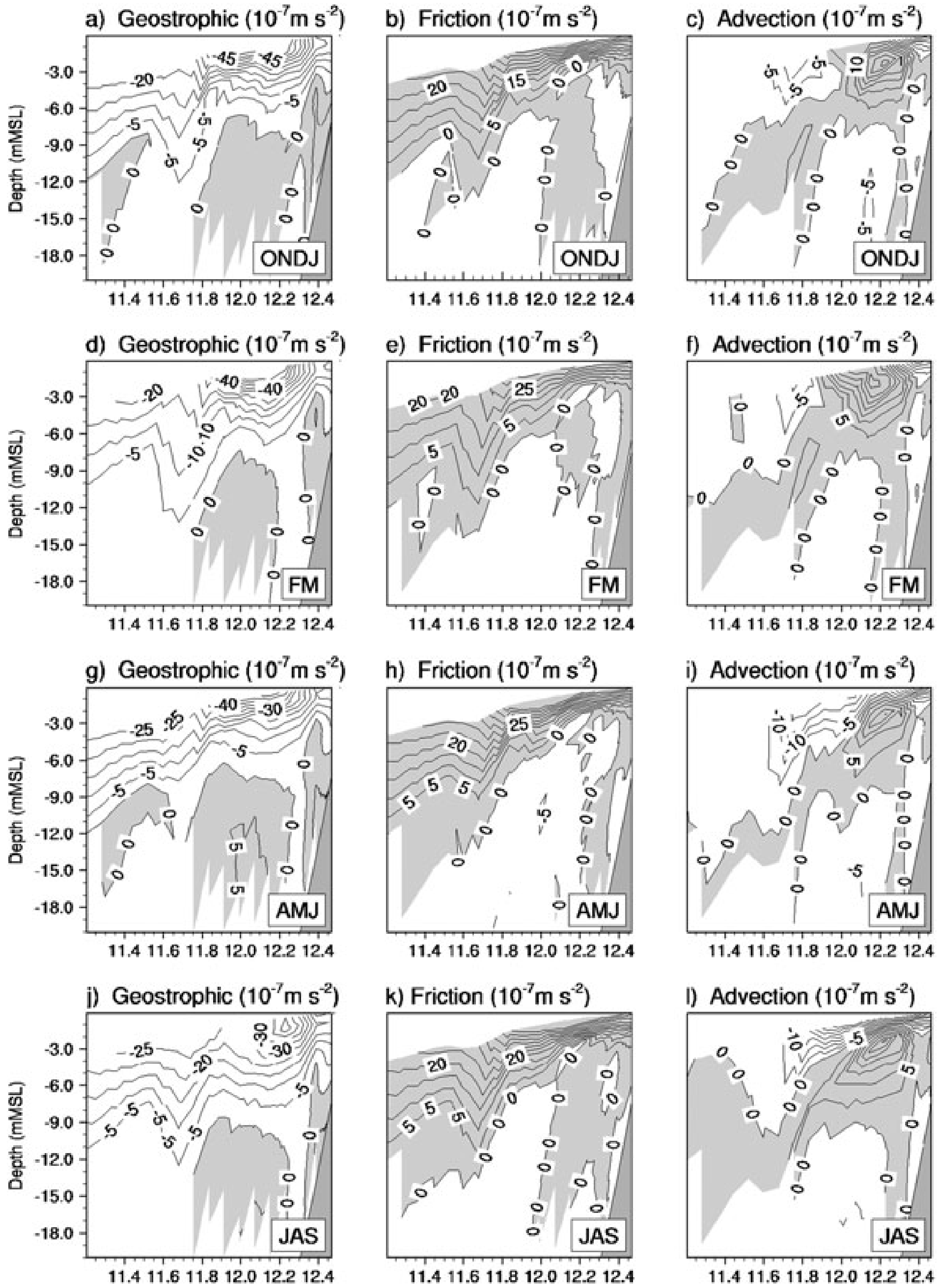

Figure 16. "Control" run—seasonal variations of the momentum balance along the 6.06°S cross-section presented for (a, d, g, and j) the geostrophic term, the (b, e, h, and k) friction term, and the (c, f, i, and l) advection.

This is a period of strong southwesterly winds favorable to northward transports which reach their maximum value for the "Baseline Wind" run. As the "Control" run northward transport remains weak, this confirms that the ambient circulation is counterbalancing the wind effects during the JAS season.

[83] At a section located south of the Congo mouth (cross-section along 6.6°S; Figure 14c), the fresh water transport variations of the "Control" run (in red) are not in phase with the ones of the "No Wind" run (in blue) but highly similar to the ones of the "Baseline Wind" run (except during January when the plume of the "Baseline Wind" run is still developing). Between March and December, the transport across this section is quasi null for the "Control" run and the "Baseline Wind" run while the "No Wind" simulation generates, on average, a $5 \times 200\ \mathrm{m^3\,s^{-1}}$ southward transport. The maximum southward transport ($Q_{fw} = 10 \times 1000\ \mathrm{m^3\,s^{-1}}$) is reached, for the "No Wind" run, at the beginning of December. Between January and April, the three runs are generating a succession of strong northward and southward

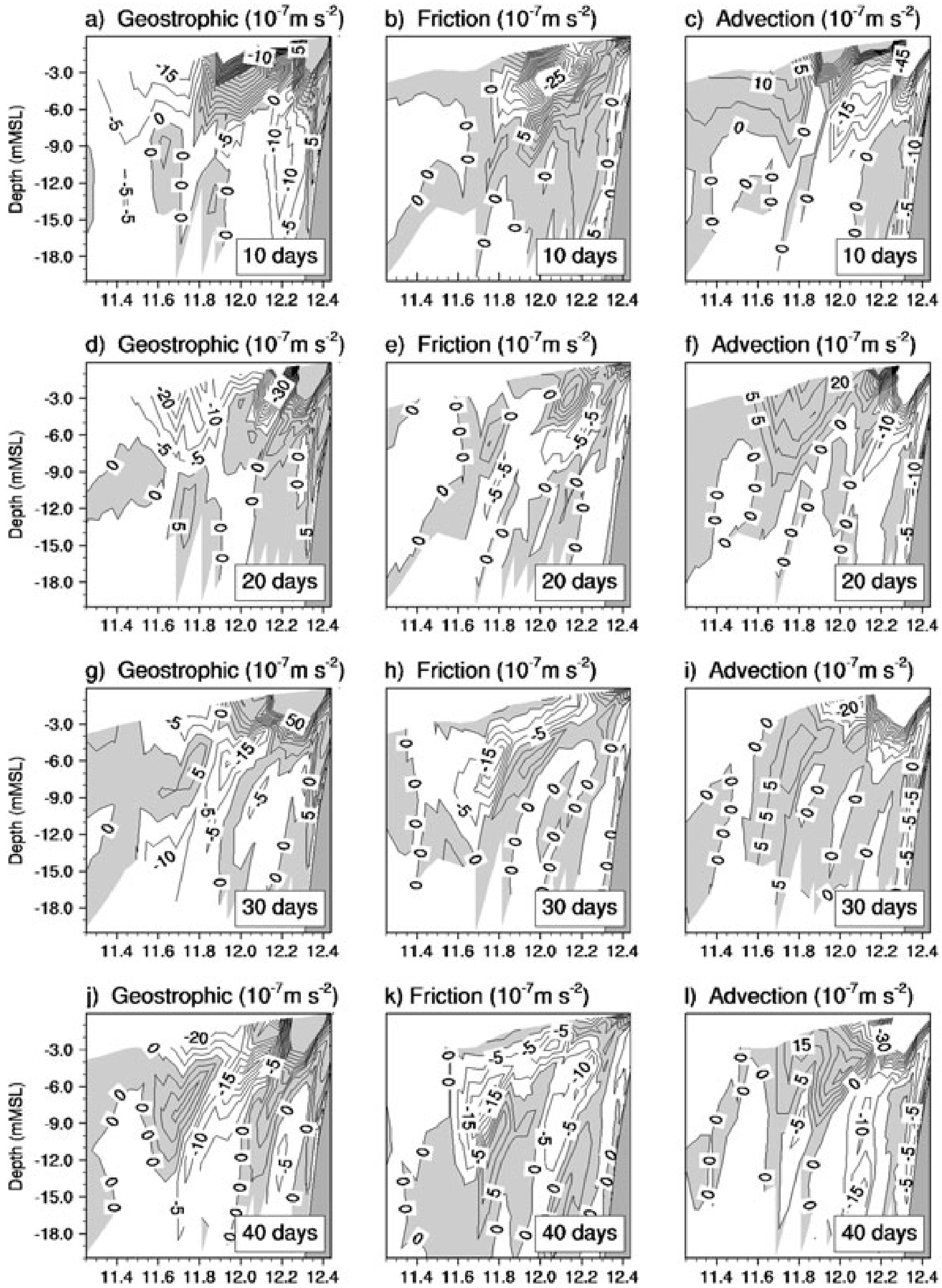

Figure 17. "Baseline" run—variations of the momentum balance along the 6.06°S cross-section presented for the (a, d, g, and j) geostrophic term, (b, e, h, and k) the friction term, and the (c, f, i, and l) advection.

transports. The maximum northward transport is reached at the end of January for the "Control" and the "No Wind" runs ($Q_{fw} = 13 \times 9000\,\mathrm{m^3\,s^{-1}}$ for the "Control" run and $Q_{fw} = 5 \times 3000\,\mathrm{m^3\,s^{-1}}$ for the "No Wind" run) and, as the "Baseline Wind" run transport is weak, it reveals the presence of a strong northward drift which can be the buoyancy-driven upstream coastal current resulting from the highest Congo River discharge (or, less likely, a nearshore branch of the BCC). The maximum southward transports of the "Control" and "Baseline Wind" runs happen at the beginning of February ($Q_{fw} = 15 \times 4000\,\mathrm{m^3\,s^{-1}}$ and $9 \times 9000\,\mathrm{m^3\,s^{-1}}$, respectively) and are due to a strong northerly wind. Nevertheless, an even stronger northerly wind event occurs at the end of March but it generates a southward transport of only $9 \times 5000\,\mathrm{m^3\,s^{-1}}$ for both the "Control" and the "Baseline Wind" runs.

[84] The variations across the last section presented Figure 14d (cross-section along 11.24°E) are representative of the behavior of the westward extension of the plume which is, as discussed in the previous sections, pronounced during the FM season (in average $Q_{fw} = 5 \times 1000\,\mathrm{m^3\,s^{-1}}$ for the "Control" run and $Q_{fw} = 2 \times 3000\,\mathrm{m^3\,s^{-1}}$ for the "No Wind" run) but weak the rest of the year. The maximum westward transport is reached at the end of March for the

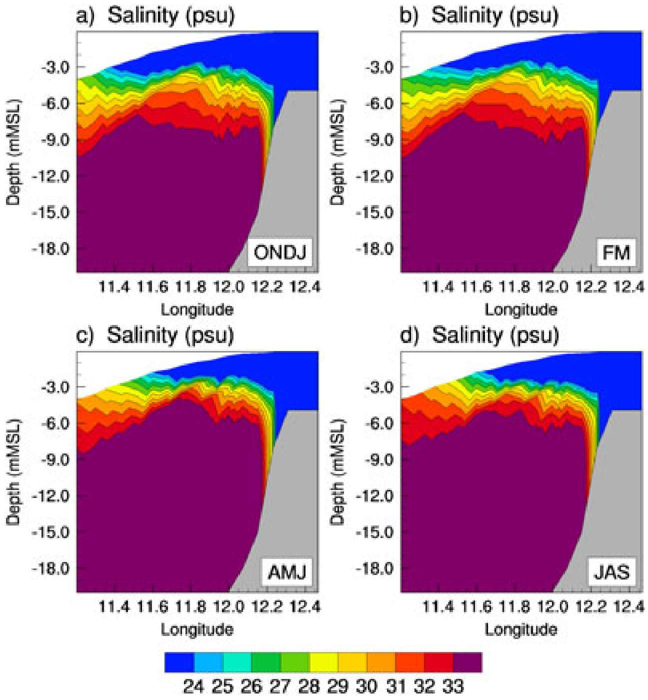

Figure 18. “No Canyon” run—seasonal variations of the salinity along the 6.06°S cross-section for (a) ONDJ, (b) FM, (c) AMJ, and (d) JAS.

“Control” run ($Q_{fw} = 12 \times 9000\,\mathrm{m}^3\,\mathrm{s}^{-1}$) and is not associated with the strongest winds. The “Baseline Wind” run presents westward transport during the entire year with maximal values reach at the end of March ($Q_{fw} = 12 \times 8000\,\mathrm{m}^3\,\mathrm{s}^{-1}$) and during November–December ($Q_{fw} = 11 \times 2000\,\mathrm{m}^3\,\mathrm{s}^{-1}$). Due to the location of the cross-section at the edge of the Congo River canyon, this westward transport seems to be related to the northwestward drift following the canyon where fresh waters are trapped (see Figures 10.2 and 11d–11g). During the ONDJ and FM seasons, a high frequency variability of eastward transports can be noticed in both the “Control” and the “Baseline Wind” runs (Figure 14d). These events mostly occur during strong northerly wind periods which generate southeastward surface currents. And as the “No Wind” run does not present any strong eastward transport, they are purely wind driven which explains their high frequency variability.

3.4. Vertical Structure of the Congo River

3.4.1. Seasonal Variations of the Near-Field Plume

[85] With the aim to characterize the vertical structure of the plume, the seasonal variations of the salinity (along the 6.06°S and 12.1°E cross-sections; see the black solid lines in Figure 1b) and the momentum balance (normal to the 6.06°S cross-section) are presented (Figures 15 and 16). The ROMS model diagnostic module allows printing out the terms of the momentum equations (horizontal and vertical advection and friction, Coriolis and pressure gradient terms calculated on the right-hand side of the equations) and thus the balance between the geostrophic effects (combined Coriolis and pressure gradient terms), the wind friction, and the advection term can be discussed. In Figures 16, 17, 19, and 21—displaying the momentum balance—the positive terms driving the northward deflection of the plume are shaded in light grey.

[86] In the vicinity of the Congo River mouth (6.06°S cross-section), the plume forms a 10 m thick fresh water layer (salinity below 33 psu) which decreases to a narrow layer of 2 m (at approximately 12.1°E) before increasing again to 5 m (see Figures 15a, 15c, 15e, and 15g). This pattern was clearly measured and described by *Eisma and Van Bennekom* [1978] and results from the entrainment of deep dense water on the surface. The strong outflow of the Congo River forced by the narrow estuary (only 14 km wide) is thus generating an upwelling of the subsurface oceanic waters. In fact, this shoaling of the pycnocline which occurs over 33 km is also showing the transition to supercritical flow associated with high values of Froude number ($F_{ul} > 1.5$; see Figure 8.3) at the head of the Congo canyon. *Armi and Farmerd* [1986] and *Hetland* [2005] explain that supercritical flows are expected for narrow estuaries which act like constrictions. However, the transition to supercritical flow of 33 km we obtained is a very gradual transition compared to the 1 km transition found by *Wright and Coleman* [1971] and *Hetland* [2005]. Moreover, a narrow band of relatively saline waters (salinity about 33 psu) is following the bottom between the estuary and 12 m of depth and the plume is already quite stratified even within the estuary of the Congo River. This behavior does not follow the near-field anatomy of the model presented by *Hetland* [2005].

[87] Off the river mouth, where the plume flows over the shelf (see 12.1°E cross-section; Figures 15b, 15d, 15f, and 15h), the fresh water surface layer thins to less than 6 m. However, it can be noticed that the plume is thinner, about 3 m, during the austral winter (AMJ and JAS seasons) than during the austral summer (ONDJ and FM seasons). It also seems that at this location the canyon does not interact with the plume.

[88] In the vicinity of the Congo River estuary (along the 6.06°S cross-section), the balance between the geostrophic effects, the friction, and the advection (see Figure 16) is clearly showing that the geostrophic term is negative in the first 10 m of depth and its effect is southward. This term controls the formation of the buoyancy-driven downstream coastal drift. In the near-field area (first 20 km from the mouth where $F_{ul} > 1$; see Figure 8.3), both surface advection term and the friction term are positive and the Rossby number (R_o which is the ratio of inertial to Coriolis force [*Kourafalou et al.*, 1996] of the supercritical flow is above 3. The advection thus plays an important role in the surface near-field northward deflection. Further offshore, the only term which remains positive on the surface is the friction term and, as the flow is subcritical ($F_{ul} \ll 1$), the wind should be the main driver of the offshore northward extension of the plume. Below 10 m of depth, where the wind friction is negligible, the northward geostrophic term is compensating by the southward effect of the advection and this behavior is probably caused by the presence of the deep canyon which decreases the friction in the vicinity of the mouth and may strongly affect the general circulation as shown by *Sutherland and Cenedese* [2009].

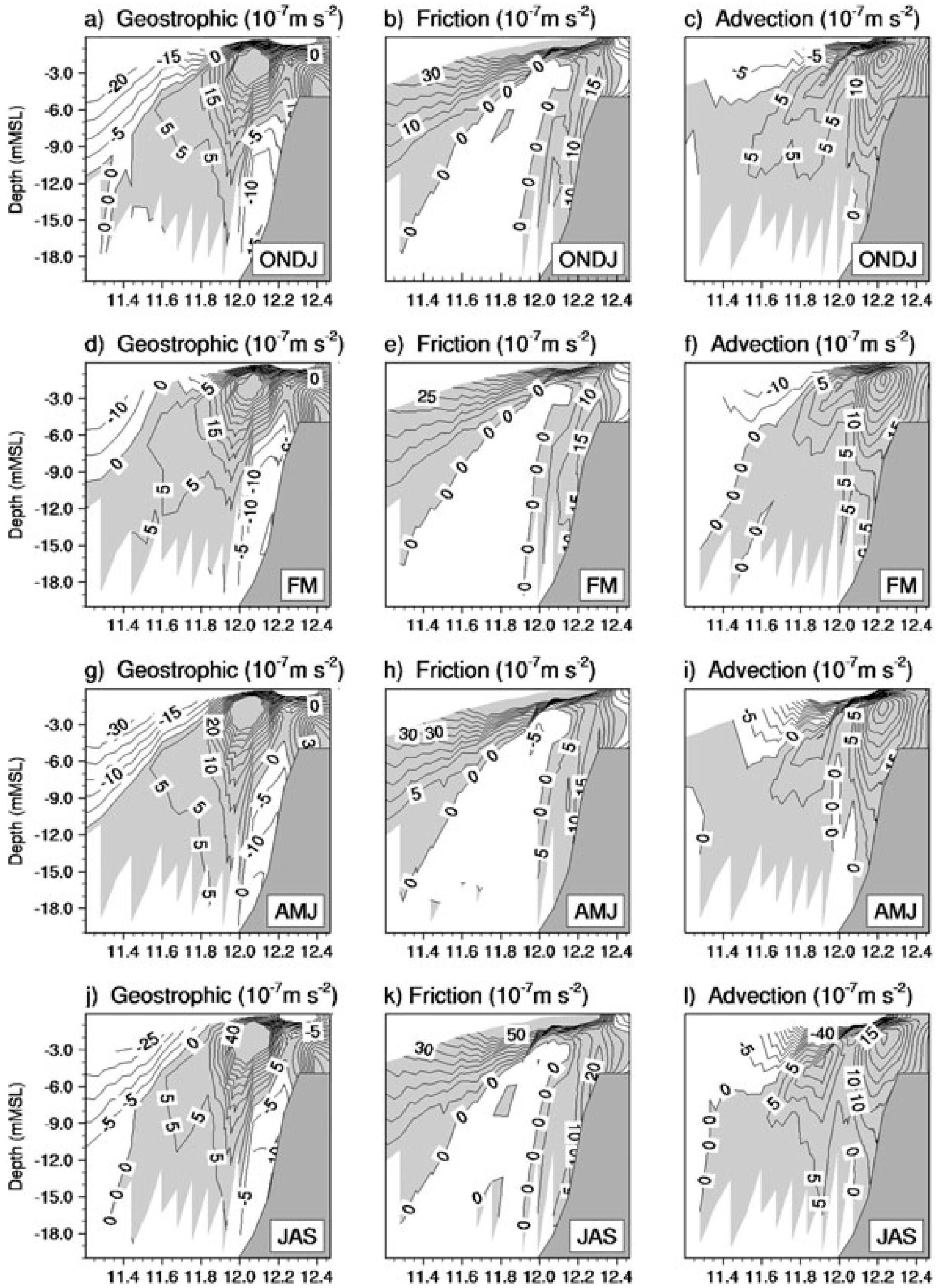

Figure 19. "No Canyon" run—seasonal variations of the momentum balance along the 6.06°S cross-section presented for the (a, d, g, and j) geostrophic term, the (b, e, h, and k) friction term, and the (c, f, i, and l) advection.

[89] The description of the morphologic and hydrographic features of the near-field region of the Congo (Zaire) plume by *Eisma and Van Bennekom* [1978] highlights the influence of two main factors: the deep Congo canyon and the tides. With the aim to characterize the respective effects of these properties, two sensitivity simulations were undertaken: a "No Tide" run without the tidal forcing included at the open boundary of the model and a "No Canyon" run with the canyon filled (in practice the bathymetry of the canyon was replaced with the results of a linear interpolation of the bathymetry between the northern and the southern edge of the canyon and an extra smoothing was applied in this region in order to prevent any spurious bathymetry effects due to the interpolation).

3.4.2. Effects of the Congo River Canyon

[90] The influence of the canyon in the near-field region is discussed according to the changes induced in the vertical structure in the vicinity of the Congo River mouth (along the 6.06°S cross-section).

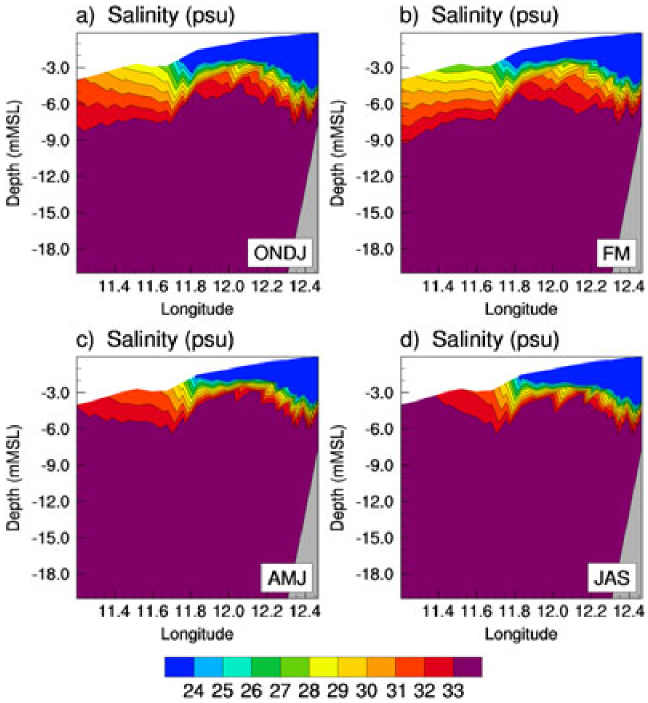

Figure 20. "No Tide" run—seasonal variations of the salinity along the 6.06°S cross-section for (a) ONDJ, (b) FM, (c) AMJ, and (d) JAS.

[91] The analysis of the "Baseline" run momentum balance gives a first assessment of the effect of the canyon on the near-field Congo River plume dynamics (see Figure 17). After 10 days (see Figures 17a–17c), when the Congo plume presents a typical evolution, the geostrophic term is generally negative in surface, except at the entrance of the estuary where a northward flow is induced by the geomorphology. The surface wind stress is null but the friction in the first 3 m below the surface is strong and negative. It thus induces a southward transport of the fresh waters. The surface advection is generally weak and positive except at the entrance of the estuary where it is strongly negative and compensates the geostrophic term. Although the geomorphology of the Congo estuary induces a buoyancy-driven upstream drift, the southward transport is clearly dominant after 10 days of simulation. In the rest of the simulation (see Figures 17d–17i), the positive geostrophic component and the negative advection—located at the entrance of the estuary—are extended and growing in intensity. However, the effects of the southward advection are weaker than the northward buoyancy induced by the geostrophic balance. The intensity of the friction is also decreasing but still has a southward effect in the first 3 m of the depth. Off the Congo River mouth (at a 30 km distance), the geostrophic and friction terms are negative and not entirely compensated by the positive advection. The downstream coastal current is thus generated 30 km further of the Congo estuary.

[92] In comparison with the "Control" run where the surface geostrophic term was always negative and the advection always positive at the entrance of the estuary, the "Baseline" run highlights the effect of the morphology of the Congo estuary: a positive geostrophic balance not entirely compensated by the negative advection and thus inducing a northward upstream current. The two main morphological features of the Congo River canyon are its depth (more than 100 m at the entrance of the estuary) and its northward orientation. The "No Canyon" experiment was thus used to discriminate the effects of depth of the canyon (which was artificially filled) from the effects of its orientation (which remains the same).

[93] The sensitivity run without the Congo canyon leads to the most dramatic changes in terms of near-field bottom salinity field of the plume (see Figure 18). The fresh water front is in agreement with the conceptual model of river plume anatomy from *Hetland* [2005]. The behavior of the plume in the "Control" run, i.e., intrusion of dense bottom water into the river mouth, can thus be explained by the presence of the deep Congo canyon penetrating into the river. In terms of the momentum balance (see Figure 19), the absence of the canyon mainly affects the advection. In the "Control" run the maximum advection is happening 5 km offshore of the estuary, but in the "No Canyon" run the maximum advection starts within the estuary and extends offshore over nearly 50 km. The Rossby number associated with the "No Canyon" run is 3.7 which is even bigger than the "Control" run and clearly highlights the importance of the advection in the vicinity of the estuary. However if the depth of the canyon dramatically affects the near-field region of the plume, it does not affect the northward fresh water transport which remains similar, along the 5.4ºS cross-section, between the runs with and without canyon (not shown). It is thus the northward orientation of the isobaths and the coastline (due to the presence of the canyon) and not the depth of the canyon which is responsible for the upstream buoyancy-driven coastal current of the Congo River plume.

3.4.3. Effects of the Tides

[94] The major net effect of the tides, at a seasonal scale and concerning the vertical structure of salinity, is the absence of the along bottom fresh water layer (lower than 33 psu and 2 m wide) that is formed between the estuary and 12 m of depth during the "Control" run (see Figures 15a, 15c, 15e, and 15g) and totally disappears in the "No Tide" run (see Figure 20). In the "No Tide" run, the water is much more stratified in the vicinity of the estuary, and during the AMJ and JAS seasons (austral winter; Figures 20c and 20d) the dense background waters are even penetrating inside the estuary. In the "Control" run, the freshwater layer is associated, along the bottom, with a narrow northward drift represented by positive geostrophic and friction terms (see Figure 16). In the vicinity of the estuary, this drift seems to strongly affect the behavior of the near-surface layer in particular during the FM and AMJ seasons (see Figures 16d, 16e, 16j, and 16k). In the "No Tide" run, along the bottom, the friction term is always negative (see Figures 21b, 21e, 21h, and 21k) and even if the geostrophic term is positive (see Figures 21a, 21d, 21g, and 21j), the northward drift is located within the bottom layer and never reaches the surface. *Pak et al.* [1984] measured an up to 1 m s^{-1} tidal current of relatively saline water moving below the surface along the north side of the estuary at a depth of −9 m. Moreover, *Eisma and Van Bennekom* [1978] indicate the presence of a net up-canyon transport due to the tides which is flushing the bottom

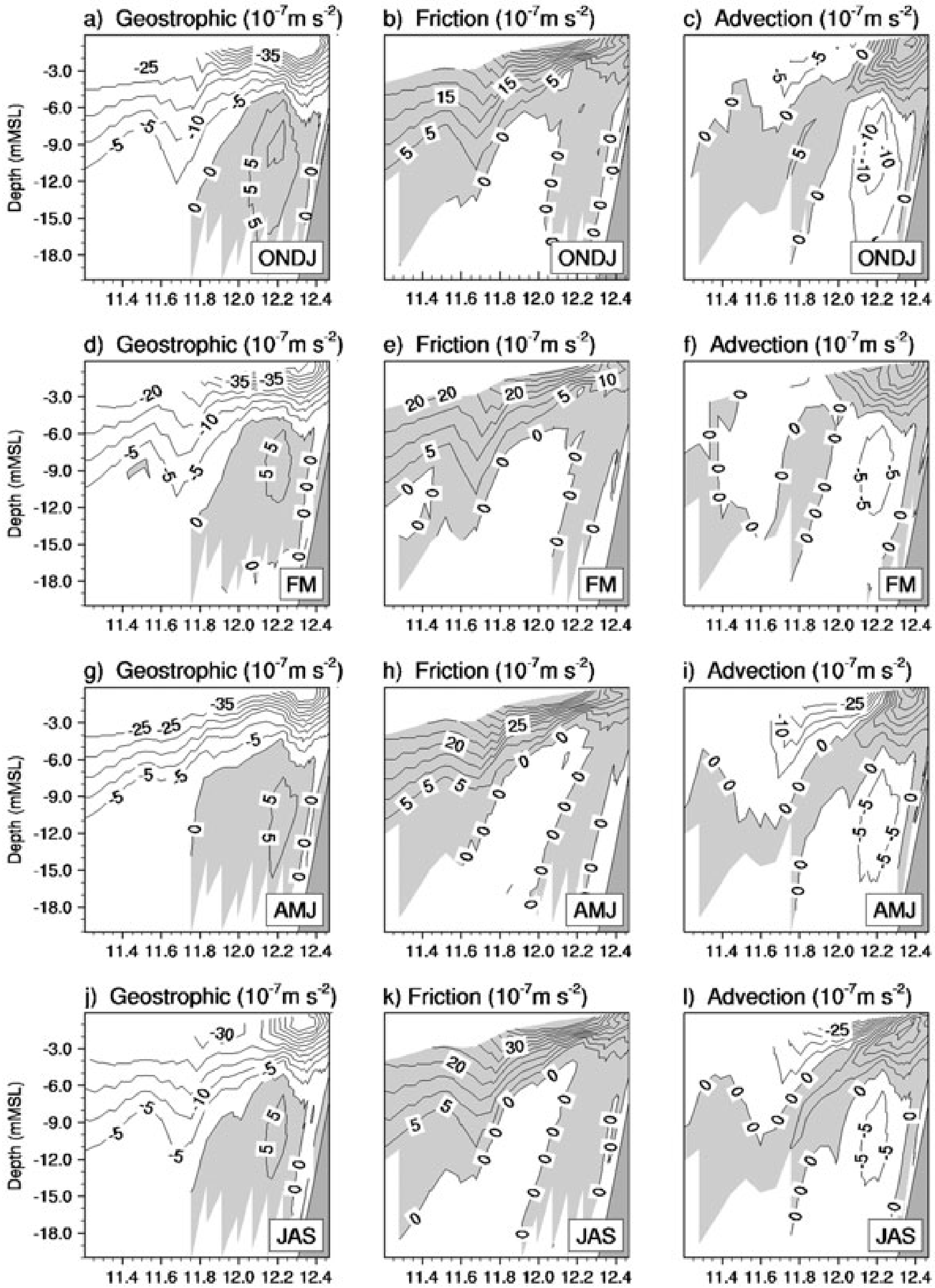

Figure 21. "No Tide" run—seasonal variations of the momentum balance along the 6.06ºS cross-section presented for the (a, d, g, and j) geostrophic term, the (b, e, h, and k) friction term, and the (c, f, i, and l) advection.

layer. This thus confirms that the net effect of the tides is to entrain fresh water along the bottom as a result of the flushing by the up-canyon transport.

4. Discussion and Conclusions

[95] Previous observations [*Eisma and Van Bennekom*, 1978; *Van Bennekom and Berger*, 1984; *Schneider et al.*, 1995; and *Signorini et al.*, 1999] have characterized the general variations of the Congo River plume. However, to the knowledge of the authors, the respective effect of each process driving the plume dynamics has not been quantified and this numerical study of the Congo River plume is the first of its kind. Our study gives a first assessment of the physical processes driving the Congo River plume far-field and near-field regions and leads to four key findings:

[96] (1) A predominantly northward surface drift of the plume induced by a strong buoyancy-driven upstream drift—due to the substantial discharge of fresh water and the unique geomorphology of the Congo River estuary—and the combined influences of the ambient ocean currents and the wind (which sometime cancel each other).

[97] (2) A large westward extension in February–March mostly driven by ambient currents.

[98] (3) An increase of the intrusion of the bottom sea water into the river mouth due to the depth of the canyon.

[99] (4) The generation, at the entrance of the estuary, of a strong buoyancy-driven upstream drift due to the orientation of the canyon.

[100] The results presented in section 3 reveal that the seasonal variations of the Congo River plume and the fresh water transport are controlled by the interdependence of various environmental conditions: the persistent wind forcing and the complex ocean circulation actively impact the far-field dynamics while the unique geomorphology of the Congo estuary drives both the far-field and the near-field plume. This study investigates the effect of each environmental factor in order to understand the processes responsible for both the northward and westward extension of a southern hemisphere river plume and the anatomy of the near-field plume.

[101] A comparison between the model and ADCP data was carried out and reveals a good performance of the model below 15 m of depth but a lack of accuracy within the surface layer where the currents of the model were generally too weak. This could be explained by the 22% underestimate of the wind speed in the forcing ERA-I fields and by the choice of the sigma level distribution or the mixing scheme. However, the quality of the measurements—obtained with a high frequency ADCP from a moving vessel and thus more influenced by small-scale phenomena—is also questionable.

[102] With respect to the far-field region dynamics, the northward fresh water transport is due to the prevalent northward buoyancy-driven drift while the westward extension of the plume can be attributed to seasonal westward ocean currents. For the near-field region, the narrow band of relatively saline waters following the bottom between the estuary and 20 m of depth was caused by the net effect of the tides. The experiment without the Congo canyon highlights the impact of the depth on sea water intrusion in the vicinity of the estuary and the impact of the canyon orientation on the far-field fresh water transport.

[103] Given the complex ocean circulation in the West African region, the HYCOM 1/12° resolution daily reanalysis data provide accurate boundary and initial conditions. Due to the size of the Congo River discharge and the narrowness of the estuary (14 km only), the choice of a 7 km resolution for the model (similar to the resolution used for the Amazon River by *Nikiema et al.* [2007] seems to be reasonable but may have affected the results in the near-field region. Moreover, although *Warner et al.*, 2005 proved the efficiency of the GLS *gen* turbulence scheme for highly stratified flow, a sensitivity study testing different mixing schemes should be carried out. The results of this study must be compared with some near-field measurements in order to select the most suitable scheme. Another important remark is that the seasonal variations of the Congo River were deduced from the model results obtain from the 2005 run, but strictly speaking several years of runs should have been used in order to provide a more accurate picture and to have a discussion on the inter-annual variability of the plume dynamics.

[104] Future work will focus on the improvement and the interaction of the different forcing and the Coupled Ocean-Atmosphere-Wave-Sediment Transport model (COAWST) [*Warner et al.*, 2010; *Kumar et al.*, 2012] which dynamically coupled the atmospheric model Weather Research and Forecasting (WRF) with the ocean model ROMS and the wave model Simulating WAves Nearshore (SWAN) and which dynamically nested grids in order to increase the resolution in the area of interest will be implemented and employed to understand the interactions between the Congo River plume, the wind waves and the swell, and the atmospheric fields.

[105] **Acknowledgments.** This presented work was supported by the BP Upstream "Environmental" Technology Program. In particular, Colin Grant is thankfully acknowledged for providing the ADCP data. The authors appreciate the support and advices from colleague Stelios Flampouris. The authors also thank the three anonymous reviewers for the insights and constructive comments they offered.

References

Armi, L., and M. Farmerd (1986), Maximal two-layer exchange through a contraction with barotropic net flow, *J. Fluid Mech.*, *164*, 27–51.
Arnault, S. (1987), Tropical Atlantic geostrophic currents and ship drifts, *J. Geophys. Res.-Oceans*, *92*(C5), 5076–5088.
Baev, S. A., and A. B. Polonsky (1991), Seasonal variability of the North Equatorial Countercurrent and North Equatorial Current in tropical Atlantic, *Okeanologiya*, *31*(2), 217–222.
Berliand, M. E., and T. G. Berliand (1952), Measurement of the effective radiation of the Earth with varying cloud amounts, *Izv. Akad. Nauk SSSR Ser. Geofiz*, *1*, 64–78.
Chao, S.-Y. (1988), Wind-driven motion of estuarine plumes, *J. Phys. Oceanogr.*, *18*(8), 1144–1166.
Chapman, D. C. (1985), Numerical treatment of cross-shelf open boundaries in a barotropic coastal ocean model, *J. Phys. Oceanogr.*, *15*(8), 1060–1075.
Chérubin, L. M., and P. L. Richardson (2007), Caribbean current variability and the influence of the Amazon and Orinoco freshwater plumes, *Deep-Sea Res. I Oceanogr. Res. Pap.*, *54*(9), 1451–1473.
Choi, B. J., and J. L. Wilkin (2007), The effect of wind on the dispersal of the Hudson River plume, *J. Phys. Oceanogr.*, *37*(7), 1878–1897.
Cummings, J. A. (2005), Operational multivariate ocean data assimilation, *Q. J. R. Meteorol. Soc.*, *131*(613), 3583–3604.
Dee, D. P., et al. (2011), The ERA-Interim reanalysis: Configuration and performance of the data assimilation system, *Q. J. R. Meteorol. Soc.*, *137*(656), 553–597.
Durand, F., F. Papa, A. Rahman, and S. K. Bala (2011), Impact of Ganges-Brahmaputra interannual discharge variations on Bay of Bengal salinity and temperature during 1992–1999 period, *J. Earth Sys. Sci.*, *120*(5), 859–872.
Egbert, G. D., and S. Y. Erofeeva (2002), Efficient inverse modeling of barotropic ocean tides, *J. Atmos. Oceanic Technol.*, *19*(2), 183–204.
Egbert, G. D., A. F. Bennett, and M. G. G. Foreman (1994), TOPEX/POSEIDON tides estimated using a global inverse model, *J. Geophys. Res.*, *99*(C12), 24,821–24,852.
Eisma, D., and J. Kalf (1984), Dispersal of Zaire River suspended matter in the estuary and the Angola basin, *Netherlands Journal of Sea Research*, *17*(2-4), 385–411.
Eisma, D., and A. J. Van Bennekom (1978), Zaire river and estuary and the Zaire outflow in the Atlantic Ocean, *Netherlands Journal of Sea Research*, *12*(3-4), 255–272.
Fairall, C. W., E. F. Bradley, D. P. Rogers, J. B. Edson, and G. S. Young (1996), Bulk parameterization of air-sea fluxes for Tropical Ocean Global Atmosphere Coupled Ocean Atmosphere Response Experiment, *J. Geophys. Res.*, *101*(C2), 3747–3764.
Flather, R. A. (1976), A tidal model of the northwest European continental shelf, in *Mémoires de la Société Royale de Sciences de Liege*, edited, pp. 141–164.
Fong, D. A., and W. R. Geyer (2002), The alongshore transport of freshwater in a surface-trapped river plume, *J. Phys. Oceanogr.*, *32*(3), 957–972.
Garvine, R. W. (1987), Estuary plumes and fronts in shelf waters: A layer model, *J. Phys. Oceanogr.*, *17*, 1877–1896.

Garvine, R. W. (1995), A dynamical system of classifying buoyant coastal discharges, *Contin. Shelf Res.*, *15*, 1585–1596.

Group, Woods Hole (2006), Met–Ocean System Observations Aboard the Drill Ship Glomar Jack Ryan Astraea-1, Hebe-1, Plutao-2, Mercurio-1, Urano-1, and Astraea-2 Wells (Angola Block 31) 23 May 2005–11 May 2006. Technical Report Submitted to BP Exploration (Angola) Limited.

Hetland, R. D. (2005), Relating river plume structure to vertical mixing, *J. Phys. Oceanogr.*, *35*(9), 1667–1688.

Jansen, J. H. F., P. Giresse, and G. Moguedet (1984), Structural and sedimentary geology of the Congo and southern Gabon continental-shelf—A seismic and acoustic reflection survey, *Netherlands Journal of Sea Research*, *17*(2–4), 364–384.

Kourafalou, V. H., L.-Y. Oey, T. N. Lee, and J. D. Wang (1996), The fate of river discharge on the continental shelf. Part II: Transport of coastal low-salinity waters under realistic wind and tidal mixing, *J. Geophys. Res.-Oceans*, *101*(C2), 3435–3455.

Kumar, N., G. Voulgaris, J. C. Warner, and M. Olabarrieta (2012), Implementation of the vortex force formalism in the coupled ocean-atmosphere-wave-sediment transport (COAWST) modeling system for inner shelf and surf zone applications, *Ocean Modelling*, *47*, 65–95.

Laraque, A., G. Mahé, D. Orange, and B. Marieu (2001), Spatiotemporal variations in hydrological regimes within Central Africa during the XXth century, *J. Hydrol.*, *245*(1–4), 104–117.

Lass, H. U., M. Schmidt, V. Mohrholz, and G. Nausch (2000), Hydrographic and current measurements in the area of the Angola-Benguela front, *J. Phys. Oceanogr.*, *30*(10), 2589–2609.

Liu, W. T., K. B. Katsaros, and J. A. Businger (1979), Bulk parameterization of air-sea exchanges of heat and water-vapor including the molecular constraints at the interface, *J. Atmos. Sci.*, *36*(9), 1722–1735.

Liu, Y., P. MacCready, B. M. Hickey, E. P. Dever, P. M. Kosro, and N. S. Banas (2009a), Evaluation of a coastal ocean circulation model for the Columbia River plume in 2004. *J. Geophys. Res.*, *114*(C2), doi:10.1029/2008JC004929.

Liu, Y., P. MacCready, and B. M. Hickey (2009b), Columbia River plume patterns in summer 2004 as revealed by a hindcast coastal ocean circulation model, *Geophys. Res. Lett.*, *36*, 2, doi:10.1029/2008GL036447.

MacCready, P., and W. R. Geyer (2001), Estuarine salt flux through an isohaline surface, *J. Geophys. Res.*, *106*(C6), 11,629–11,637.

MacCready, P., N. S. Banas, B. M. Hickey, E. P. Dever, and Y. G. Liu (2009), A model study of tide- and wind-induced mixing in the Columbia River Estuary and plume, *Cont. Shelf Res.*, *29*(1), 278–291.

MacDonald, D. G., L. Goodman, and R. D. Hetland (2007), Turbulent dissipation in a near-field river plume: A comparison of control volume and microstructure observations with a numerical model, *J. Geophys. Res.*, *112*(C7), C07026, doi:10.1029/2006JC004075

Marchesiello, P., J. C. McWilliams, and A. F. Shchepetkin (2001), Open boundary conditions for long-term integration of regional ocean models, *Ocean Modelling*, *3*, 1–20.

Maritorena, S., O. Hembise Fanton d'Andon, A. Mangin, and D. A. Siegel (2010), Merged satellite ocean color data products using a bio-optical model: Characteristics, benefits and issues, *Remote. Sens. Environ.*, *114*(8), 1791–1804.

Mazeika, P. A. (1967), Thermal domes in the eastern Atlantic Ocean, *Limnol. Oceanogr.*, *12*, 537–539.

McClain, C. R., and J. Firestone (1993), An investigation of Ekman upwelling in the North-Atlantic, *J. Geophys. Res.-Oceans*, *98*(C7), 12,327–12,339.

Mittelstaedt, E. (1991), The ocean boundary along the northwest African coast—Circulation and oceanographic properties at the sea-surface, *Prog. Oceanogr.*, *26*(4), 307–355.

Moroshkin, K. V., V. A. Bunov, and R. P. Bulatov (1970), Water circulation in the eastern South Atlantic Ocean, *Oceanology*, *10*, 27–34.

Nikiema, O., J. L. Devenon, and M. Baklouti (2007), Numerical modeling of the Amazon River plume, *Cont. Shelf Res.*, *27*(7), 873–899.

O'Donnell, J., S. G. Ackleson, and E. R. Levine (2008), On the spatial scales of a river plume, *J. Geophys. Res.*, *113*(C4), C04017, doi:10.1029/2007JC004440.

Orlanski, I. (1976), A simple boundary condition for unbounded hyperbolic flows, *J. Comput. Phys.*, *21*(3), 251–269.

Pak, H., J. R. V. Zaneveld, and R. W. Spinrad (1984), Vertical-distribution of suspended particulate matter in the Zaire river, estuary and plume, *Netherlands Journal of Sea Research*, *17*(2-4), 412–425.

Raymond, W. H., and H. L. Kuo (1984), A radiation boundary-condition for multi-dimensional flows, *Q. J. R. Meteorol. Soc.*, *110*(464), 535–551.

Reynolds, R. W., N. A. Rayner, T. M. Smith, D. C. Stokes, and W. Q. Wang (2002), An improved in situ and satellite SST analysis for climate, *J. Clim.*, *15*(13), 1609–1625.

Reynolds, R. W., T. M. Smith, C. Liu, D. B. Chelton, K. S. Casey, and M. G. Schlax (2007), Daily high-resolution-blended analyses for sea surface temperature, *J. Clim.*, *20*(22), 5473–5496.

Richardson, P. L., and D. Walsh (1986), Mapping climatological seasonal-variations of surface currents in the tropical Atlantic using ship drifts, *J. Geophys. Res.*, *91*(C9), 537–550.

Salisbury, J., D. Vandemark, J. Campbell, C. Hunt, D. Wisser, N. Reul, and B. Chapron (2011), Spatial and temporal coherence between Amazon River discharge, salinity, and light absorption by colored organic carbon in western tropical Atlantic surface waters, *J. Geophys. Res. Oceans*, *116*, C00H02.

Schiller, R. V., V. H. Kourafalou, P. Hogan, and N. D. Walker (2011), The dynamics of the Mississippi River plume: Impact of topography, wind and offshore forcing on the fate of plume waters, *J. Geophys. Res.*, *116*, C06029, doi:10.1029/2010JC006883.

Schneider, R. R., P. J. Muller, and G. Ruhland (1995), Late Quaternary surface circulation in the east equatorial South-Atlantic—Evidence from Alkenone sea-surface temperatures, *Paleoceanography*, *10*(2), 197–219.

Shchepetkin, A. F., and J. C. McWilliams (2005), The regional oceanic modeling system (ROMS): A split-explicit, free-surface, topography-following-coordinate oceanic model, *Ocean Model.*, *9*(4), 347–404.

Signorini, S. R., R. G. Murtugudde, C. R. McClain, J. R. Christian, J. Picaut, and A. J. Busalacchi (1999), Biological and physical signatures in the tropical and subtropical Atlantic, *J. Geophys. Res.*, *104*(C8), 18,367–18,382.

Smith, W. H. F., and D. T. Sandwell (1997), Global seafloor topography from satellite altimetry and ship depth soundings, *Science*, *277*, 1957–1962.

Smolarkiewicz, P. K. (1983), A simple positive definite advection scheme with small implicit diffusion, *Mon. Weather. Rev.*, *111*(3), 479–486.

Smolarkiewicz, P. K. (1984), A fully multidimensional positive definite advection transport algorithm with small implicit diffusion, *J. Comput. Phys.*, *54*(2), 325–362.

Smolarkiewicz, P. K., and T. L. Clark (1986), The multidimensional positive definite advection transport algorithm—Further development and applications, *J. Comput. Phys.*, *67*(2), 396–438.

Smolarkiewicz, P. K., and W. W. Grabowski (1990), The multidimensional positive definite advection transport algorithm—Non-oscillatory option, *J. Comput. Phys.*, *86*(2), 355–375.

Sutherland, D. A., and C. Cenedese (2009), Laboratory experiments on the interaction of a buoyant coastal current with a canyon: Application to the East Greenland Current, *J. Phys. Oceanogr.*, *39*(5), 1258–1271.

Umlauf, L., and H. Burchard (2003), A generic length-scale equation for geophysical turbulence models, *J. Mar. Res.*, *61*(2), 235–265.

Van Bennekom, A. J., and G. W. Berger (1984), Hydrography and silica budget of the Angola basin, *Netherlands Journal of Sea Research*, *17*(2-4), 149–200.

Vörösmarty, C. J., B. Fekete, and B. A. Tucker (1998), River Discharge Database, Version 1.1 (RivDIS v1.0 Supplement). Available through the Institute for the Study of Earth, Oceans, and Space, University of New Hampshire, Durham NH (USA), edited.

Warner, J. C., W. R. Geyer, and J. A. Lerczak (2005), Numerical modeling of an estuary: A comprehensive skill assessment, *J. Geophys. Res.*, *110*(C5), C05001, doi:10.1029/2004jc002691.

Warner, J. C., C. R. Sherwood, H. G. Arango, and R. P. Signell (2005), Performance of four turbulence closure models implemented using a generic length scale method, *Ocean Model.*, *8*(1-2), 81–113.

Warner, J. C., B. Armstrong, R. Y. He, and J. B. Zambon (2010), Development of a coupled ocean-atmosphere-wave-sediment transport (COAWST) modeling System, *Ocean Modelling*, *35*(3), 230–244.

Wedepohl, P. M., J. R. E. Lutjeharms, and J. M. Meeuwis (2000), Surface drift in the South-East Atlantic Ocean, *South African Journal of Marine Science-Suid-Afrikaanse Tydskrif Vir Seewetenskap*, *22*, 71–79.

Wiseman, W. J., and R. W. Garvine (1995), Plumes and coastal currents near large river mouths, *Estuaries*, *18*(3), 509–517.

Wright, L. D., and J. M. Coleman (1971), Effluent expansion and interfacial mixing in the presence of a salt wedge, Mississippi River Delta, *J. Geophys. Res.-Oceans*, *76*(36), 8649–8661.